

## OBSERVATIONAL CONSTRAINTS ON CORRELATED STAR FORMATION AND ACTIVE GALACTIC NUCLEI IN LATE-STAGE GALAXY MERGERS

R. SCOTT BARROWS<sup>1</sup>, JULIA M. COMERFORD<sup>1</sup>, NADIA L. ZAKAMSKA<sup>2</sup>, MICHAEL C. COOPER<sup>3</sup>

<sup>1</sup>Department of Astrophysical and Planetary Sciences, University of Colorado Boulder, Boulder, CO 80309, USA;  
Robert.Barrows@Colorado.edu

<sup>2</sup>Department of Physics and Astronomy, Johns Hopkins University, Bloomberg Center, 3400 N. Charles St., Baltimore, MD 21218, USA  
and

<sup>3</sup>Center for Galaxy Evolution, Department of Physics and Astronomy, University of California, Irvine, 4129 Frederick Reines Hall, Irvine, CA 92697, USA

*Accepted for publication in ApJ*

### ABSTRACT

Galaxy mergers are capable of triggering both star formation and active galactic nuclei (AGN) and therefore may represent an important pathway in the co-evolution of galaxies and supermassive black holes (SMBHs). However, correlated enhancements of merger-induced star formation and AGN triggering may be hidden by the variable conditions and timescales during which they occur. In Paper I, we presented evidence of merger-triggered AGN in a sample of six late-stage galaxy mergers (2–8 kpc nuclear separations). In this follow-up work, we use multi-wavelength *Hubble Space Telescope* imaging and additional archival data to examine their star-forming properties to test for merger-triggered star formation, and if it is correlated with SMBH growth. We find that the morphological asymmetries are correlated with enhanced specific star formation rates, indicating the presence of merger-triggered star formation. Additionally, the stellar populations become younger with increasing radius from the nucleus, indicating that the merger-induced star formation primarily occurs on global scales. However, we also find that the star formation rate enhancements are consistent with or lower than those of larger separation galaxy pair samples. This result is consistent with simulations predicting a decline of the global star formation rates in late-stage galaxy mergers with < 10 kpc nuclear separations. Finally, we find that enhancements in specific star formation rate and AGN luminosity are positively correlated, but that an average temporal delay of  $\gtrsim 10^8$  years likely exists between the peak of global star formation and the onset of AGN triggering in 80% of the systems.

*Subject headings:* galaxies: active - galaxies: evolution - galaxies: interactions - galaxies: Seyfert - galaxies: star formation

### 1. INTRODUCTION

Galaxy mergers can efficiently trigger star formation (SF) and accretion onto supermassive black holes (SMBHs) that power active galactic nuclei (AGN). While this scenario is likely secondary to that of secular processes for the triggering of most low-luminosity AGN (e.g. in Seyfert galaxies), evidence persists that the most massive SMBHs are grown (in quasar phases) within the most massive galaxies. In this case, a co-evolutionary framework is defined by mergers between massive gas-rich galaxies that are an efficient means of growing both SMBHs and their host galaxy stellar populations. Specifically, merger-induced torques on gas and dust result in both enhanced accretion onto the nuclear SMBHs and enhanced SF (Hernquist 1989; Barnes & Hernquist 1991; Mihos & Hernquist 1996; Springel et al. 2005a; Hopkins et al. 2008; Capelo et al. 2016). This results in a buildup of SMBH mass that tracks the buildup of stellar mass. Indeed, higher luminosity AGN are associated with younger stellar populations (Kauffmann et al. 2003; Wild et al. 2007) and increased SF (Heckman et al. 2004; Madau & Dickinson 2014), while empirical correlations between SMBH masses and stellar bulges do suggest such a proportionality (Gebhardt et al. 2000; Ferrarese & Merritt 2000; Marconi & Hunt 2003; Gültekin et al. 2009; Bentz et al. 2009). The merger pathway also predicts the overall demographics of SMBH host galaxies in which the

most massive SMBHs tend to be found in massive elliptical galaxies composed of old stellar populations that are likely the result of gas-rich mergers (Hopkins et al. 2005, 2008; Heckman & Best 2014).

Individual on-going examples of galaxy-SMBH co-evolution are seen in local ultra-luminous infrared galaxies that contain both rapid SF rates (SFRs) and AGN (Sanders et al. 1988a,b; Canalizo & Stockton 2001). Additionally, statistical inferences made with large samples suggest that galaxy mergers drive the growth of the most massive SMBHs and the SF in their host galaxies (Rosario et al. 2012). Other studies have shown that decreasing galaxy pair separations correspond to increases in both the merger fraction of AGN samples (Ellison et al. 2011; Satyapal et al. 2014) and SFRs in star-forming galaxies (Patton et al. 2011; Scudder et al. 2012; Patton et al. 2013). However, observationally detecting directly correlated enhancements in SF and SMBH accretion among samples of individual galaxy mergers has proven difficult. In particular, while the relevance of galaxy mergers for triggering enhanced SF has been robustly established observationally (Joseph & Wright 1985; Jogee et al. 2009; Engel et al. 2011; Knapen & Cisternas 2015; Knapen et al. 2015), a corresponding case for AGN triggering is currently tenuous since some existing results favor a connection (Treister et al. 2012; Comerford & Greene 2014; Glikman et al. 2015; Barrows et al. 2017) while others do not (Georgakakis et al. 2009; Ko-

cevski et al. 2012; Simmons et al. 2012; Villforth et al. 2014; Mechtley et al. 2015; Villforth et al. 2016).

The lack of a clear connection between SF and AGN in galaxy mergers may be due to the different environmental conditions in which they are triggered. In particular, while observations suggest that the AGN merger fraction is preferentially enhanced in major versus minor mergers (Ellison et al. 2011; Comerford et al. 2015; Barrows et al. 2017), a similar dependence on mass ratio is not clear for merger-triggered SF. Some studies have shown that merger-induced SF is strongly negatively correlated with merger mass ratio (Somerville et al. 2001; Cox et al. 2008; Ellison et al. 2008) such that higher SFRs are seen in major (as opposed to minor) mergers that are more effective at introducing morphological disturbances and randomizing stellar orbits that dynamically evolve galaxies toward early-types (Guo et al. 2016). On the other hand, minor mergers are theoretically capable of triggering starbursts (Mihos & Hernquist 1994), and observations show that the SF in both major and minor galaxy mergers appears to be similarly enhanced relative to the star-forming main sequence (Willett et al. 2015). Moreover, a significant fraction of SF in the local Universe may occur in galaxies with implicit signs of past minor mergers such as early-type galaxies featuring dust lanes (Shabala et al. 2012) and spiral galaxies with disturbed morphologies (Kaviraj 2014). Indeed, Woods & Geller (2007) show that the conditions for merger-induced SF are more dependent on the strength of the tidal interaction force relative to the galaxy’s self gravity rather than merger mass ratio.

Observations of galaxy mergers reveal SF on both nuclear scales (Keel et al. 1985; Sanders et al. 1988a; Duc et al. 1997) and global scales (Cullen et al. 2006; Elmegreen et al. 2006; Smith et al. 2008; Hancock et al. 2009). However, the correlation with AGN may be strongest for nuclear SF due to a common dependence on the nuclear gas supply. Therefore, the physical extent over which the measured SF is integrated can affect the statistical significance of correlations with AGN. For example, one set of simulations finds a statistically significant positive correlation between nuclear ( $< 100$  pc radii) SFR and SMBH accretion rates (Volonteri et al. 2015). However, when including SF on larger physical scales ( $< 5$  kpc radii), they find a much weaker correlation. When examining the *global* SF, the only statistically significant connections with AGN appear during late-stage galaxy mergers when the SMBH accretion rates and SFRs are both large and generate similar luminosities (Rosario et al. 2012; Volonteri et al. 2015). This prediction is borne out observationally as SMBH accretion only appears correlated with *nuclear* SF (Davies et al. 2007; Diamond-Stanic & Rieke 2012).

Finally, the level of correspondence between global SF and SMBH accretion in galaxy mergers may be affected by the relative chronology of the two. Observationally, temporal delays between the peak of SFRs and SMBH accretion rates have been identified from AGN residing in host galaxies with relatively old stellar populations. For example, Schawinski et al. (2009) estimate a time delay of  $\sim 100$  Myr between the peak luminosity of X-ray selected AGN and the onset of the decline in SFR, while Wild et al. (2010) find that the rise in SMBH accretion rate among optically selected AGN oc-

curs  $\sim 250$  Myr after the starburst begins. The reported delays are even longer for radio selected AGN and have been estimated at more than 400 Myr (Shabala et al. 2017) or several galaxy dynamical timescales (Kaviraj et al. 2015a,b).

Numerical simulations that study the evolution of merger dynamics have produced results that are roughly consistent with these observed temporal delays for SF measured over both large (kpc-scale) and small (pc-scale) spatial extents (Hopkins 2012). In general, simulations of galaxy mergers find that while the SMBH accretion rate is relatively unaffected until a steep rise after the second pericentric passage that corresponds to nuclear separations of  $< 10$  kpc (Di Matteo et al. 2005; Springel et al. 2005b; Capelo et al. 2015), the SF experiences a strong peak near the first pericentric passage (Cox et al. 2008; Hopkins et al. 2008; Kim et al. 2009; Teyssier et al. 2010; Scudder et al. 2012; Stickley & Canalizo 2014; Renaud et al. 2014), and on global scales declines gradually throughout the entire subsequent merger process (Capelo et al. 2015). On the other hand, the nuclear SF rises most strongly after the second pericentric passage, accounting for the temporal correspondence seen between merger-triggered SF and AGN in simulations (Di Matteo et al. 2005; Springel et al. 2005b; Hopkins et al. 2008; Capelo et al. 2015). Since the stellar populations age after each pericentric passage when the galaxy separations increase (Patton et al. 2011), the stellar populations are assembled over a much larger fraction of the merger time-frame than the SMBH growth. As a result, the majority of the merger-induced SF is completed at nuclear separations of  $> 30$  kpc (Patton et al. 2013), thereby producing the measured several hundred Myr ages of the stellar populations once the AGN is observed (Schawinski et al. 2007, 2009; Kaviraj 2014; Shabala et al. 2017). This sequence of stellar and SMBH evolution can account for the fact that SFR enhancements in mergers are seen out to galaxy separations of  $\sim 150$  kpc (Patton et al. 2013) whereas the enhancement of the AGN merger fraction occurs only below  $\sim 80$  kpc (Ellison et al. 2011; Satyapal et al. 2014).

Observationally testing these predictions requires a sample of galaxy mergers with sufficient spatial resolution to resolve late galaxy merger stages when AGN are more likely to be triggered, measure morphological disturbances, study the distribution of SF at both nuclear and global physical scales, and estimate SF histories. In Comerford et al. (2015), hereafter Paper I, we used a sample of AGN observed with the *Hubble Space Telescope* (*HST*) and *Chandra* to find hints of merger-driven AGN triggering in a sample of late-stage galaxy mergers (2 – 8 kpc nuclear separations). In particular, we found that the frequency with which accretion onto both SMBHs of the progenitor galaxies is triggered tends to be higher for more luminous AGN, in major mergers, and at small nuclear separations. In this work, we search for evidence of merger-driven SF and examine how it is related to properties of the host galaxy and the AGN. Ultimately, we place our results within the context of galaxy-SMBH co-evolution. The paper is structured as follows: in Section 2 we describe the galaxy sample and datasets; in Section 3 we describe the spectral analysis; in Section 4 we describe the image analysis; in Section 5 we describe the results; in Section 6 we discuss the results as they pertain

to connections between galaxy mergers, SF, and AGN; and in Section 7 we present our conclusions. Throughout we assume a cosmology defined by  $H_0 = 70 \text{ km s}^{-1} \text{ Mpc}^{-1}$ ,  $\Omega_M = 0.3$ , and  $\Omega_\Lambda = 0.7$ .

## 2. SAMPLE

The sample analyzed in this work consists of six galaxy mergers hosting AGN (one Type 1 AGN and five Type 2 AGN) and that span a redshift ( $z$ ) range of  $z = 0.102 - 0.339$ . The AGN classifications are based on the presence of broad emission lines for Type 1 AGN or narrow emission line ratio diagnostics for Type 2 AGN (Baldwin et al. 1981; Kewley et al. 2006). The Type 1 AGN (J0952+2552) was drawn from the SDSS DR7 Quasar Catalog (Schneider et al. 2010). Of the five Type 2 AGN, four (J0841+0101, J1126+2944, J1239+5314, and J1322+2631) were drawn from the MPA-JHU value-added catalog of physical properties for galaxies and AGN<sup>1</sup> (Kauffmann et al. 2003; Brinchmann et al. 2004), and the fifth (J1356+1026) was drawn from a catalog of Type 2 quasars (Reyes et al. 2008). These six systems are a subset of a dual AGN candidate sample selected based on double-peaked narrow AGN emission lines (primarily [O III] $\lambda$ 5007) in their optical Sloan Digital Sky Survey (SDSS) spectra, a feature that may represent the orbital motion of two AGN narrow line regions (NLRs). From that spectroscopic sample, ten of those double-peaked systems were selected for follow-up imaging with the *HST* Wide Field Camera 3 in the three filters F160W ( $H$ ), F814W ( $I$ ) and F438W ( $B$ ) and for observations with the *Chandra X-ray Observatory*.

The analysis in Paper I used the *HST* imaging to spatially resolve the nuclear regions in search of dual stellar cores and used the *Chandra* data to spatially constrain the locations of AGN within the systems. Paper I addressed the interacting nature of these systems, considering a system to be a merger if two galaxy stellar cores are apparent from modeling of the  $H$ -band images, finding the above six systems to be galaxy mergers. In Paper I, AGN were identified as *Chandra* detections being spatially coincident with an [O III] $\lambda$ 5007 detection and a galaxy stellar core. Merger systems in which only one AGN is spatially identified are referred to as offset AGN and systems in which two AGN are spatially identified are referred to as dual AGN. The analysis in Paper I found one system that satisfies the dual AGN criteria (J1126+2944) and five that satisfy the offset AGN criteria (J0841+0101, J0952+2552, J1239+5314, J1322+2631, and J1356+1026).

Due to the initial spectroscopic selection and the selection of bright follow-up *Chandra* targets, these AGN are biased toward high [O III] $\lambda$ 5007 luminosities relative to the parent samples from which they were drawn. Based on their integrated [O III] $\lambda$ 5007 luminosities from Paper I, the three faintest systems (J1126+2944, J1239+5314, and J1322+2631) have  $L_{[\text{OIII}]} = 3 - 5 \times 10^{41} \text{ erg s}^{-1}$  and are comparable to Seyfert galaxies, while the three brightest systems (J0841+0101, J0952+2552, and J1356+1026) have  $L_{[\text{OIII}]} = 2 - 5 \times 10^{42} \text{ erg s}^{-1}$  and are comparable to quasars (Sanders & Mirabel 1996).

In this paper, we use the three *HST* filter images for

a separate analysis of merger morphologies and galaxy colors. We augment the *HST* imaging with photometric data from the Galaxy Evolution Explorer (*GALEX*; Martin et al. 2003), the SDSS, and the Wide-field Infrared Survey Explorer (*WISE*; Wright et al. 2010) for spectral energy distribution (SED) modeling and with SDSS optical fiber spectra for synthesized stellar population modeling.

## 3. SPECTRAL ANALYSIS

In this section we describe our analysis of the broadband and optical spectra of the six merging systems. In Section 3.1 we fit galaxy and AGN templates to the broadband photometric SEDs to measure star formation rates and stellar masses. In Section 3.2 we fit synthesized stellar templates to the SDSS optical fiber spectra to measure ages of the stellar populations. The physical components included in both the broadband and optical spectral modeling consist of the host galaxy stellar continuum, the AGN continuum, broadened emission lines (in the case of Type 1 AGN), narrow emission lines, and a nuclear obscuring medium. Contribution from the additional components of AGN-heated dust in the mid-IR (MIR), scattered AGN continuum emission in the UV, and line emission from spatially large NLRs are considered separately. In Section 3.3 we build matched control samples for use in our subsequent analysis.

### 3.1. Star Formation Rates and Stellar Masses

We build the broadband SEDs using flux densities from three surveys that have observed each galaxy. The highest energy bandpasses are from the *GALEX* Kron aperture magnitudes in the Far-UV ( $\lambda_{\text{eff.}} = 1516 \text{ \AA}$ ) and Near-UV ( $\lambda_{\text{eff.}} = 2267 \text{ \AA}$ ) detectors. They are followed by the SDSS Data Release 7 (DR7) model magnitudes in the  $u'$  ( $\lambda_{\text{eff.}} = 3561 \text{ \AA}$ ),  $g'$  ( $\lambda_{\text{eff.}} = 4718 \text{ \AA}$ ),  $r'$  ( $\lambda_{\text{eff.}} = 6185 \text{ \AA}$ ),  $i'$  ( $\lambda_{\text{eff.}} = 7499 \text{ \AA}$ ), and  $z'$  ( $\lambda_{\text{eff.}} = 8961 \text{ \AA}$ ) filters. The lowest energy bandpasses are from the *WISE* profile-based magnitudes in the  $W1$  ( $\lambda_{\text{eff.}} = 3.4 \text{ \mu m}$ ),  $W2$  ( $\lambda_{\text{eff.}} = 4.6 \text{ \mu m}$ ),  $W3$  ( $\lambda_{\text{eff.}} = 12.1 \text{ \mu m}$ ), and  $W4$  ( $\lambda_{\text{eff.}} = 22.2 \text{ \mu m}$ ) channels. The choice of these three surveys (up to a combined eleven photometric datapoints covering  $\sim 0.15$  to  $\sim 22 \text{ \mu m}$ ) is to assemble data over most of the  $0.03 - 30 \text{ \mu m}$  range covered by our SED models (described below). All six galaxies are detected in all the filters of each survey, with the exception of *GALEX* for which there are no Far-UV detections of two systems (J1126+2944 and J1322+2631). In these cases we confirm that the SED model sum does not predict flux greater than the Far-UV sensitivity upper limit at  $\lambda_{\text{eff.}} = 1516 \text{ \AA}$ . Since the templates do not extend below  $0.03 \text{ \mu m}$ , we do not include *Chandra* detections in our SED models.

We model each SED using the Low-Resolution Templates (LRT) program (Assef et al. 2010). LRT models a broadband SED as a linear combination of galaxy templates (elliptical, Sbc Spiral, and Irregular) plus a Type 1 AGN template. The AGN template was developed by Assef et al. (2010) as a combination of power laws plus broad emission lines and is designed to resemble the composite Type 1 quasar template from Richards et al. (2006). A wavelength-dependent extinction law constructed from the Cardelli et al. (1989) optical-IR

<sup>1</sup> <http://www/mpa.mpa-garching.mpg.de/SDSS/>

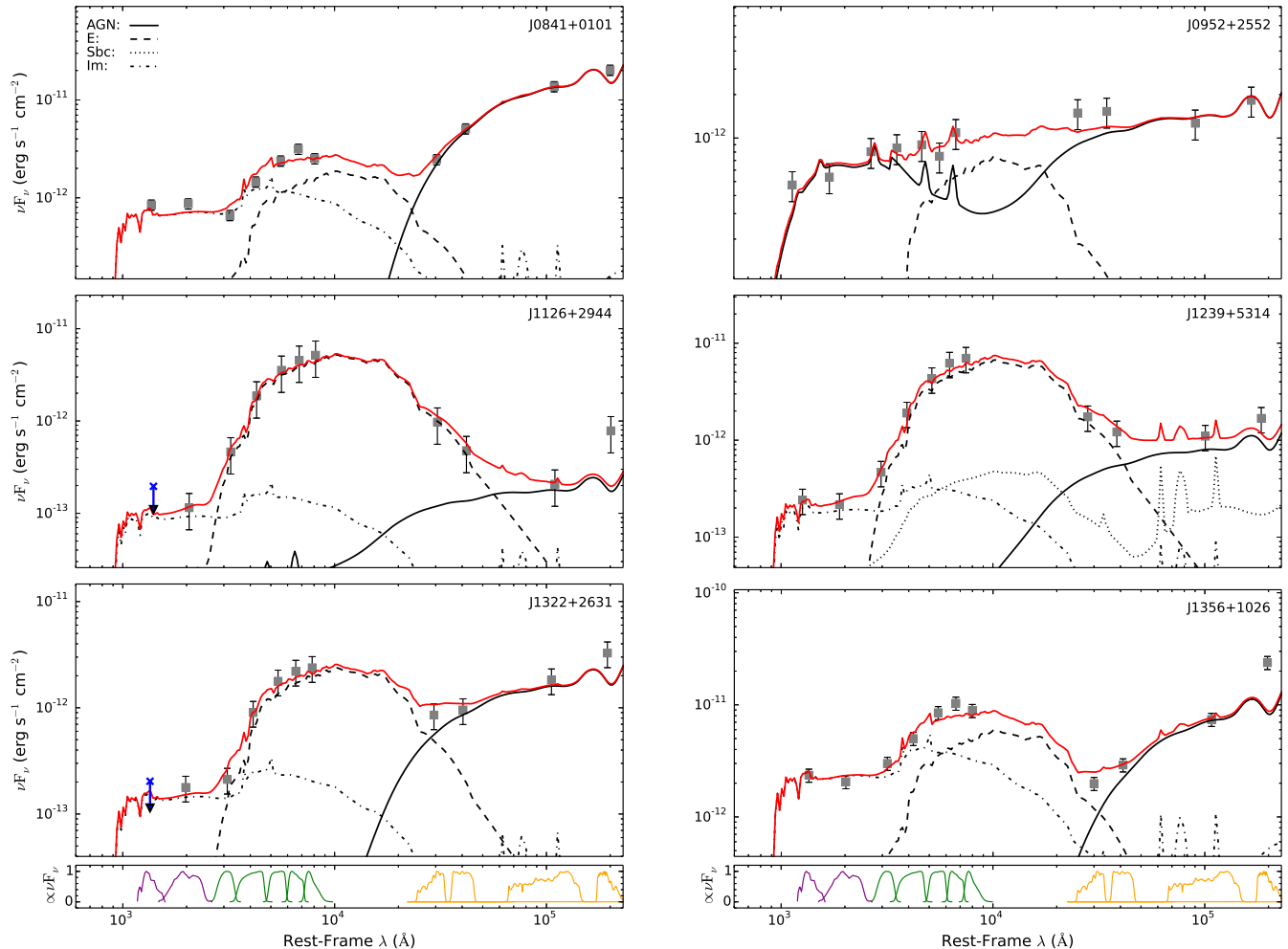


**Figure 1.** Rest-frame SEDs of the six merging systems with photometric data points (shown as gray squares) from *GALEX* (Far-UV and Near-UV), SDSS ( $u'$ ,  $g'$ ,  $r'$ ,  $i'$ , and  $z'$ ) and *WISE* ( $W1$ ,  $W2$ ,  $W3$ , and  $W4$ ). The data points are plotted at the filter effective wavelength with their  $1\sigma$  upper and lower uncertainties shown. The filter response curves are shown in the bottom of each panel for *GALEX* (purple), SDSS (green) and *WISE* (orange). For each system, the best-fit model sum is shown by the red, solid line. The individual components of the best-fit model are also shown as black lines: AGN with obscuration applied (solid), Elliptical galaxy (dashed), Sbc galaxy (dotted) and Im galaxy (dashed-dotted). For galaxies with no *GALEX* FUV detection (J1126+2944 and J1322+2631), the downward arrows indicate the sensitivity upper limit.

function (for  $\lambda > 3300\text{\AA}$ ) and the Gordon & Clayton (1998) UV function (for  $\lambda < 3300\text{\AA}$ ) is also applied to the AGN template. This extinction term,  $E(B-V)_{\text{AGN,SED}}$ , effectively accounts for nuclear obscuration and thereby suppresses both the continuum and narrow/broad emission lines of the AGN template. With sufficient extinction, the optical and UV portion of the final SED will resemble that of a Type 2 AGN. We note that, in the case of the dual AGN system (J1126+2944), the two AGN likely experience different levels of nuclear obscuration. However, the two AGN components and their extinction terms are strongly degenerate and we do not have the spectral resolution to deblend them. Therefore, we only include the single extinguished AGN component and note that the nuclear obscuring solution likely reflects a value intermediate to that of the two AGN. The SEDs and best fit models are shown in Figure 1.

We sum the best-fit elliptical, Sbc Spiral, and Irregular galaxy templates to measure the rest-frame monochromatic UV ( $2800\text{\AA}$ ) luminosity ( $\nu L_{\nu}[2800\text{\AA}]$ ) of each

galaxy assuming the SDSS spectroscopic redshift and the cosmology stated in Section 1. Then assuming a Salpeter initial mass function we use  $\nu L_{\nu}[2800\text{\AA}]$  and the UV-based relation of Madau et al. (1998) to estimate star formation rates ( $\text{SFR}_{\text{SED}}$ ). We also use the summed galaxy flux to measure the host galaxy stellar masses ( $M_{\star,\text{SED}}$ ) using the  $g'-r'$  color,  $M/L_g$  relation of Bell et al. (2003), and the  $g'$ - and  $r'$ -band  $k$ -corrections from our SED models. We then combine  $\text{SFR}_{\text{SED}}$  with  $M_{\star,\text{SED}}$  to estimate specific star formation rates ( $\text{sSFR}_{\text{SED}} = \text{SFR}_{\text{SED}}/M_{\star,\text{SED}}$ ). In Table 1 we list  $E(B-V)_{\text{AGN,SED}}$ ,  $\text{SFR}_{\text{SED}}$ ,  $M_{\star,\text{SED}}$ , and  $\text{sSFR}_{\text{SED}}$ .

### 3.1.1. Additional Sources of Emission

In this section we consider additional sources of emission that are not explicitly included in the SED models but may contribute to the broadband photometry and affect our estimates of  $\text{SFR}_{\text{SED}}$  and  $M_{\star,\text{SED}}$ . In particular, we consider scattered AGN continuum flux, emission line flux from extended NLRs, and flux from AGN-heated dust.

*Scattered light:* While the nuclear continuum source and broad line region are obscured from direct view in Type 2 AGN, a fraction of that light can be scattered into the line-of-sight (Antonucci & Miller 1985; Kishimoto 1999). The flux due to electron and dust scattering rises toward and peaks in the rest-frame UV (Kishimoto et al. 2001; Draine 2003), and in powerful Type 2 quasars the scattering regions can reach several kpc in size (Zakamska et al. 2005). As a result, the UV contribution to the SED from scattered flux at large radii may be significant for the more powerful AGN in our sample. The degree of scattering is parameterized by the scattering efficiency: the ratio of scattered flux to that of the intrinsic source (Zakamska et al. 2006). Since scattered flux in AGN hosts at UV wavelengths is a strong function of the intrinsic AGN luminosity, we estimate the scattered flux at 3000 Å assuming a typical scattering efficiency of 3% (Obied et al. 2016).

To quantify the effect of scattered light on our measurements of  $\text{SFR}_{\text{SED}}$  and  $M_{\star, \text{SED}}$ , we extrapolate the scattered flux to all wavelengths assuming a power-law function ( $F_{\lambda} \sim \lambda^{-\alpha}$ ) with  $\alpha = 1.5$  (Vanden Berk et al. 2001). Relative to the overall SED flux at 2800 Å, we find scattered light fractions of 88.81%, 6.25%, 3.32%, 8.41%, 35.85%, and 15.17% for J0841+0101, J0952+2552, J1126+2944, J1239+5314, J1322+2631, and J1356+1026. These values are qualitatively similar to the lower limits found for the sample of more luminous Type 2 quasars from Zakamska et al. (2006) in the F550W filter. Relative to the overall flux in the  $g'$ -band, we find significantly lower scattered light fractions of 8.13%, 1.47%, 0.07%, 0.23%, 1.31%, and 1.40% for J0841+0101, J0952+2552, J1126+2944, J1239+5314, J1322+2631, and J1356+1026. Since the scattered light affects the 2800 Å measurements by factors of 4 – 40 more than the  $g'$ -band measurements, the  $\text{SFR}_{\text{SED}}$  values are likely significantly more over-estimated than those of  $M_{\star, \text{SED}}$ , contributing to over-estimates of  $\text{sSFR}_{\text{SED}}$ .

*AGN-heated dust:* A dusty obscuring medium is expected to reprocess AGN continuum emission, thereby contributing to excess MIR flux not accounted for by the Type 1 AGN template. Indeed, we see that the SED model significantly under-predicts the  $W_4$  photometry in some of the systems by 37.32–74.59%. Three of the four systems with the most under-predicted  $W_4$  fluxes correspond to the three highest values of  $E(B-V)_{\text{AGN, SED}}$ , while the system with the least under-predicted  $W_4$  flux corresponds to the lowest value of  $E(B-V)_{\text{AGN, SED}}$ . Additionally, after removing J1126+2944 (which hosts two AGN whose separate nuclear obscuring components are not accounted for; Section 3.1), the values of  $E(B-V)_{\text{AGN, SED}}$  are inversely correlated with the  $W_4$  model under-predictions with a Spearman rank statistic of  $r = 0.70$  and null-hypothesis probability of  $p = 0.18$ . This connection between excess MIR flux and nuclear extinction is consistent with AGN continuum emission that is absorbed and reradiated by the nuclear obscuring medium. Furthermore, this signature of relatively steeply rising MIR flux is also seen in Wylezalek et al. (2016), who find that simple models of dust distributions leave significant excess flux at rest-frame wavelengths of  $> 10 \mu\text{m}$  and conclude that it is primarily due to dust heated by the central AGN.

However, this effect is negligible in the  $W_3$  band (96.51–99.18) and at similar levels in all higher energy bands. Therefore, we assume that the contribution from AGN heated dust does not significantly affect the modeled fluxes at higher energies and hence the modeled AGN component normalization (used for our scattered flux estimates) is accurate.

*Emission lines:* NLRs are expected to extend beyond the nuclear obscuring medium and therefore suffer less attenuation than the broad emission lines. However, suppression of the AGN template in the SED modeling also suppresses the modeled NLR contribution without accounting extended NLR emission that is not subject to obscuration. Furthermore, the SED modeling does not account for NLRs of above average luminosity (e.g. from powerful AGN or enhanced by AGN outflows/shocks). Therefore, to estimate the actual flux contributions of each narrow emission line to the photometry, we separately convolved the galaxy continuum and narrow emission line components that are accessible in the SDSS optical spectra with the filters used in the SED modeling to produce synthetic magnitudes for each. The ratio of narrow emission line flux to total galaxy flux in each filter represents the maximum contribution of the narrow emission lines to each filter.

Emission lines from extended or powerful NLRs may be contributing to excess flux and causing the SED to over-estimate the galaxy components. The emission line contributions to the  $g'$ -band due to the  $[\text{O III}]\lambda 5007 + \text{H}\beta$  complex are  $< 0.02\%$ . While we do not have spectral access to rest-frame UV emission lines and can not estimate their direct contributions to  $\nu L_{\nu}[2800\text{\AA}]$ , they are likely negligible since the  $\text{Mg II}\lambda 2800$  line is confined to the broad line region. The overall emission line contribution may be stronger than our estimates since the MPA-JHU catalog values are normalized to the fiber magnitudes (i.e. they do not include an aperture correction) so that the emission line contributions estimated from the optical spectra may be under-estimates for the whole systems if extended NLRs are present. For example, J1356+1026 is known to contain a large-scale AGN-driven outflow of ionized gas in *HST* imaging that extends beyond the SDSS fiber (Greene et al. 2014). However, since our estimates of emission line contributions within the fiber are negligible, any further contribution from extended emission is likely to be negligible as well. Therefore, the emission line contributions are smaller than those of scattering in both the  $g'$ -band and at 2800 Å, leading to the result that the effects of scattering are likely to dominate over those of emission lines.

### 3.1.2. Comparison Measurements

For comparison, we also obtained measurements made with the SDSS optical fiber spectra ( $M_{\star, \text{SDSS}}$  and  $\text{SFR}_{\text{SDSS}}$ ) for the four galaxies in our sample in the MPA-JHU catalog. Stellar masses in the MPA-JHU catalog ( $M_{\star, \text{SDSS}}$ ) are generated by fitting a grid of models from Bruzual & Charlot (2003) to the broadband SDSS photometry. For AGN, measurements of  $\text{sSFR}_{\text{SDSS}}$  are based on the 4000 Å break (D4000) and the empirical correlation between D4000 and  $\text{sSFR}$  calibrated from star-forming galaxies in Brinch-

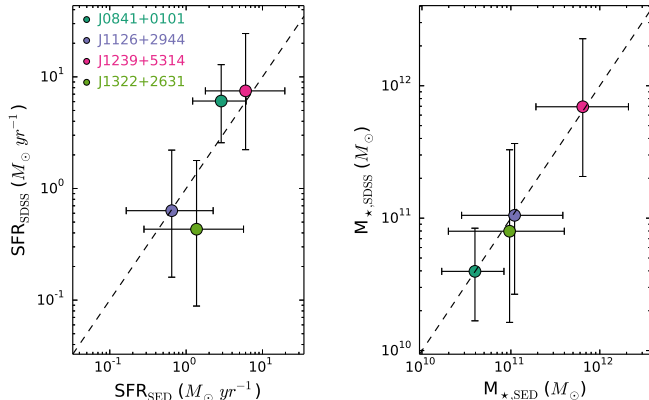


**Figure 2.** Left: SFR estimates from SED modeling versus from the SDSS. Right:  $M_*$  estimates from SED modeling versus from the SDSS. In each panel the dashed line represents the one-to-one relation. Note that the values from SED modeling and from the SDSS are consistent within  $1\sigma$  among values of SFR and  $M_*$ , though the scatter is larger for the former.

mann et al. (2004). We compute values of  $\text{SFR}_{\text{SDSS}}$  as  $\text{SFR}_{\text{SDSS}} = \text{sSFR}_{\text{SDSS}} \times M_{*,\text{SDSS}}$ .

Figure 2 compares the values of SFR and  $M_*$  from the UV-based SED method against those of the optical-based SDSS method. From the left panel of Figure 2, we see that the values of  $\text{SFR}_{\text{SED}}$  are well-correlated with those of  $\text{SFR}_{\text{SDSS}}$ , consistent within their uncertainties and with an average offset from unity of 36%. For comparison, with a substantially larger sample Lee et al. (2009) find that, for SFR above  $0.1 M_{\odot} \text{ yr}^{-1}$  (which is the case for all measurements of SFR in our six merger systems, regardless of method), the average offset from unity is 30%. The agreement within 6% indicates the robustness of our measurements. From the right panel of Figure 2, we see that the values of  $M_{*,\text{SED}}$  are well-correlated with those of  $M_{*,\text{SDSS}}$ , consistent within their uncertainties and with an average offset from unity of 8%. Therefore, the differences between  $\text{sSFR}_{\text{SED}}$  and  $\text{sSFR}_{\text{SDSS}}$  are dominated by the differences in their respective SFR values.

The UV-based SED method is sensitive to longer SF timescales of 100 Myr compared to the optical-based SDSS method sensitivity to timescales of 10 Myr (Lee et al. 2009). In our subsequent analysis, we adopt the SFR and  $M_*$  estimates from SED modeling ( $\text{SFR}_{\text{SED}}$  and  $M_{*,\text{SED}}$ ) since they do not involve applying an aperture correction, they account for the presence of an AGN continuum, the broad-band photometry covers a much larger range in energy, and we have measurements for all six systems.  $\text{SFR}_{\text{SED}}$ ,  $M_{*,\text{SED}}$ , and  $\text{sSFR}_{\text{SED}}$  are shown in Table 1. For completeness, we also include in Table 1  $\text{SFR}_{\text{SDSS}}$ ,  $M_{*,\text{SDSS}}$ , and  $\text{sSFR}_{\text{SDSS}}$ .

### 3.2. Stellar Ages

The SDSS fiber spectra has observed spectral coverage of  $3800 - 9200 \text{ \AA}$ , and the rest-frame spectral coverage of our sample ranges from  $3440 - 8340 \text{ \AA}$  (lowest redshift system) to  $2840 - 6870 \text{ \AA}$  (highest redshift system). We used STARLIGHT (Cid Fernandes et al. 2004) to model the fiber spectra with synthesized stellar templates while masking resolved emission lines. Over the rest-frame wavelength coverage of the SDSS, the physical components that may contribute to the spectra consist of

the host galaxy stellar continuum, AGN continuum, and broad/narrow emission lines. However, as shown in Section 3.1 an AGN component is only significant at optical wavelengths in Type 1 AGN. Therefore, AGN continuum and broadened Fe II pseudo-continuum components are also included for the Type 1 AGN (J0952+2552). Section 3.1 also shows that reprocessed emission from dust only becomes significant at IR wavelengths while scattered AGN continuum light only becomes significant at UV wavelengths. Therefore, these components are not considered in our optical spectral modeling.

For the stellar populations, we used a library of 45 bases from Bruzual & Charlot (2003) that span three different metallicities ( $Z = [0.004, 0.02, 0.05]$ ) and 15 different ages ( $t_{\text{age,SDSS}} = [0.001 - 13] \times 10^9 \text{ yr}$ ). We applied a freely varying extinction curve (Cardelli et al. 1989) with  $R_V = 3.1$  to the stellar bases. To include the AGN continuum for J0952+2552, we added to the library a power-law base defined by  $F_{\lambda} = 10^{20} (\lambda/4020 \text{ \AA})^{-\alpha} \text{ erg s}^{-1} \text{ cm}^{-2} \text{ \AA}^{-1}$  as in Mezcua et al. (2011). For the power-law index  $\alpha$ , we investigated the results using six discrete values:  $\alpha = -[0.5, -1.0, -1.5, -2.0, -2.5, -3.0]$ . We applied a separate freely varying extinction curve to the power-law base representing the AGN. When varying  $\alpha$  over the six values, we find that the values of  $t_{\text{age,SDSS}}$  are all consistent within their respective uncertainties. Therefore, we adopted the value of  $\alpha = -1.5$  as in Section 3.1.1. We also added to its library a base of empirically derived Fe II pseudo-continuum created from the templates of Véron-Cetty et al. (2004) and Tsuzuki et al. (2006). When including the Fe II component, the best-fit combination of stellar bases is dominated by the youngest population ( $t_{\text{age,SDSS}} = 10^6 \text{ yrs}$ ). Therefore, we consider this  $t_{\text{age,SDSS}}$  value to be a lower limit. The optical fiber spectra and best fit models are shown in Figure 3. We then computed mean stellar ages ( $t_{\text{age,SDSS}}$ ) as the mass-weighted average age of the individual stellar populations. Values of  $t_{\text{age,SDSS}}$  are listed in Table 1.

### 3.3. Building the Control Sample

To understand the values of SFR,  $M_*$ , and  $t_{\text{age,SDSS}}$  for our sample within the context of the AGN population, we build control samples for each merger system. To do so, we matched these six merger systems to AGN (selected based on the same narrow emission line ratios from Section 2) in the MPA-JHU galaxy catalogue on values of  $M_*$ ,  $z$ , and  $L_{[\text{OIII}]}$ . We included galaxies in control samples if matches on  $M_*$ ,  $z$ , and  $L_{[\text{OIII}]}$  are within the thresholds of 20%, 20%, and 50%, respectively, as used in Nevin et al. (2017). This ensures that control samples for the four AGN originally selected from the MPA-JHU catalog (J0841+0101, J1126+2944, J1239+5314, and J1322+2631) include at least 10 sources. The other two (J0952+2552 and J1356+1026) are both classified as quasars (Type 1 and Type 2, respectively) and therefore are more luminous than the other four. J1356+1026 requires matches to  $L_{[\text{OIII}]}$  to be within 75% to provide at least 10 sources in the control sample. J0952+2552 requires matches to  $L_{[\text{OIII}]}$  to be within 100%, plus an increase to 50% for matches on  $M_*$  and  $z$  to provide at least 10 sources in the control sample. The final numbers in each control sample are 18 (J0841+0101), 10 (J0952+2552), 175 (J1126+2944), 20 (J1239+5314),

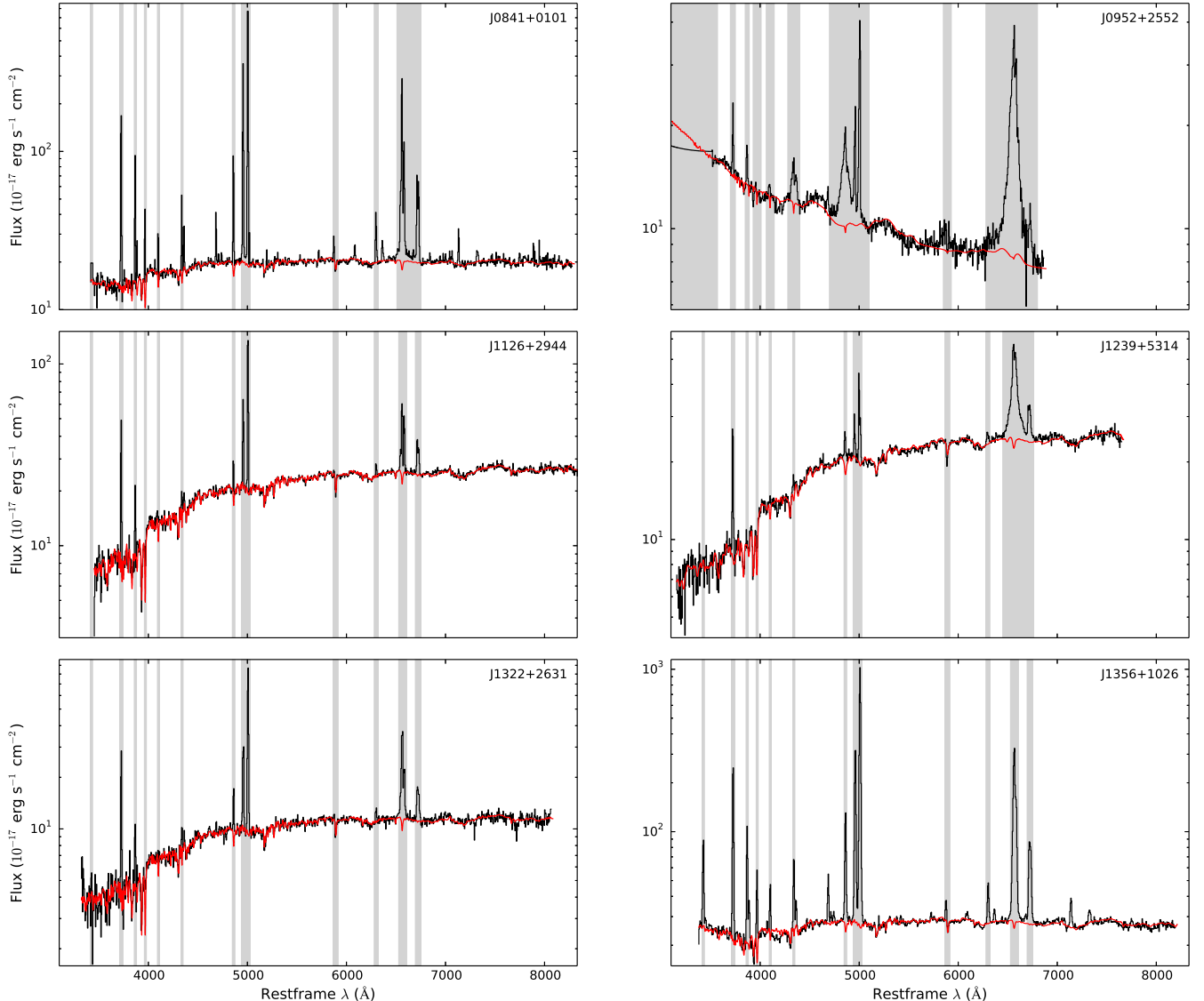


**Figure 3.** Rest-frame SDSS fiber spectra of the six merging systems (black, solid lines). The flux-weighted sum of the best-fit combination of 45 stellar bases is shown by the red, solid line. Spectral regions that were masked during the fitting (based on emission lines and bad pixels) are shown with gray shading. All spectra are shown over the same rest-frame wavelength range chosen so as to display the full SDSS spectrum for each source.

310 (J1322+2631), and 14 (J1356+1026). We ran the LRT SED modeling procedure (using the same photometric surveys as in Section 3.1) and the STARLIGHT spectral modeling procedure (using the SDSS optical fiber spectra as in Section 3.2) on all galaxies from each control sample. Finally, we computed the average values for each control sample to obtain  $\text{SFR}_{\text{ctrl}}$ ,  $M_{\star, \text{ctrl}}$ , and  $t_{\text{age, ctrl}}$ .

As discussed in Section 3.1.1, light from scattering, extended NLRs, and AGN-heated dust can contribute to the photometry beyond the SED modeling capabilities. While we have shown that the effects of emission lines and heated dust are likely to be small, scattered AGN continuum emission can elevate our measurements of  $\text{sSFR}_{\text{SED}}$  to artificially high levels. This effect will also occur among the AGN in the control samples and will affect comparisons if the average AGN luminosity of the control sample (which dominates the scattering contribution) is significantly different from that of the AGN

to which it is matched. Based on  $L_{[\text{OIII}]}$ , we find that the AGN luminosities of the six merger systems are greater than the average of the matched control samples by factors of 2.16–7.80. This implies that the over-estimates of  $\text{sSFR}_{\text{SED}}$  in the six merger systems are more significant than in the control samples in all cases. The implications of this effect are considered in Sections 5.2 and 5.3.

#### 4. IMAGE ANALYSIS

In this Section we describe our analysis of the imaging data for the six merging systems. In Section 4.1 we fit two-dimensional parametric models to the  $H$ -band images to model the spatial distribution of the stars and assess the presence of morphological disturbances. In Section 4.2 we characterize the radial color gradients to quantify the spatial distribution of young stellar populations.

**Table 1**  
Host galaxy properties derived from broadband and optical spectral modeling

SDSS Name	$t_{\text{age,SDSS}}$	$E(B-V)_{\text{AGN,SED}}$	$\text{SFR}_{\text{SED}}$	$M_{\star,\text{SED}}$	$s\text{SFR}_{\text{SED}}$	$\text{SFR}_{\text{SDSS}}$	$M_{\star,\text{SDSS}}$	$s\text{SFR}_{\text{SDSS}}$
—	(log[yr])	(mag)	( $M_{\odot} \text{ yr}^{-1}$ )	(log[ $M_{\odot}$ ])	(log[ $\text{yr}^{-1}$ ])	( $M_{\odot} \text{ yr}^{-1}$ )	(log[ $M_{\odot}$ ])	(log[ $\text{yr}^{-1}$ ])
(1)	(2)	(3)	(4)	(5)	(6)	(7)	(8)	(9)
J0841+0101	$9.89^{0.20}_{0.36}$	$8.8^{9.8}_{5.1}$	$2.9^{3.2}_{1.7}$	$10.60^{0.34}_{0.42}$	$-10.14^{0.35}_{0.43}$	$6.1^{6.8}_{3.5}$	$10.60^{0.33}_{0.38}$	$-9.81^{0.33}_{0.37}$
J0952+2552	$> 6.00^{\text{a}}$	$0.1^{0.0}_{0.0}$	$2.3^{0.2}_{0.2}$	$12.21^{0.05}_{0.05}$	$-11.86^{0.04}_{0.05}$	—	—	—
J1126+2944	$10.03^{0.16}_{0.26}$	$0.4^{1.1}_{0.3}$	$0.6^{1.6}_{0.5}$	$11.04^{0.57}_{0.74}$	$-11.23^{0.52}_{0.50}$	$0.6^{1.6}_{0.5}$	$11.02^{0.55}_{0.61}$	$-11.22^{0.54}_{0.58}$
J1239+5314	$9.91^{0.20}_{0.39}$	$1.4^{3.2}_{1.0}$	$6.0^{13.6}_{4.2}$	$11.81^{0.53}_{0.59}$	$-11.03^{0.51}_{0.51}$	$7.5^{17.0}_{5.3}$	$11.84^{0.49}_{0.46}$	$-10.97^{0.54}_{0.62}$
J1322+2631	$9.98^{0.18}_{0.30}$	$4.0^{12.5}_{3.2}$	$1.4^{4.3}_{1.1}$	$10.99^{0.63}_{0.79}$	$-10.85^{0.63}_{0.74}$	$0.4^{1.3}_{0.3}$	$10.90^{0.63}_{0.78}$	$-11.27^{0.63}_{0.77}$
J1356+1026	$10.08^{0.17}_{0.28}$	$10.2^{1.0}_{1.0}$	$11.9^{1.2}_{1.2}$	$11.20^{0.04}_{0.05}$	$-10.12^{0.04}_{0.05}$	—	—	—

**Note.** — Column 1: abbreviated SDSS galaxy name; Column 2: mass-weighted mean age of the stellar populations from optical spectra modeling; Column 3: color excess of the AGN template from broadband SED modeling; Columns 4-6: star formation rate, stellar mass, and specific star formation rate from broadband SED modeling; Column 7-9: star formation rate, stellar mass, and specific star formation rate from optical spectral modeling.

<sup>a</sup> Poorly constrained due to the presence of Fe II emission.

#### 4.1. Morphological Disturbances

From Section 3.1 we see that all six merger systems have small flux contributions in the  $H$ -band (peak wavelength of 15450 Å and  $FWHM = 2900$  Å) from scattered light ( $<0.41\%$ ), and no measurable contribution from emission lines and AGN-heated dust. We see that five of the systems (J0841+0101, J1126+2944, J1239+5314, J1322+2631, and J1356+1026) have small flux contributions in the  $H$ -band from AGN light (0.14–2.85%). While the remaining system (J0952+2552) is a Type 1 AGN with a stronger AGN contribution (41.66%), the AGN flux is from the continuum and therefore is likely confined to the central four pixels (based on the  $H$ -band PSF) so that it contributes negligibly to the global  $H$ -band morphology. Therefore, the  $H$ -band galaxy images are dominated by light from stellar continuum emission. This flux corresponds to stellar populations with spectral curves peaking at NIR wavelengths and hence relatively older stars (Mannucci et al. 2001) that represent the classical bulge components of galaxies.

To model the  $H$ -band images of the merger systems, we fit each with a combination of multiple Sersic functions. The Sersic function (Sersic 1968) is a reliable model for a wide range of stellar light radial profiles (Graham & Driver 2005), with the freely varying exponential parameter  $n$  (Sersic index) describing how light is concentrated around the peak. Smaller values of  $n$  tend toward more concentrated profiles with smooth peaks, while larger values of  $n$  tend toward more extended profiles with cuspy peaks. The Sersic function is widely used to model stellar bulges of galaxies, either in elliptical galaxies or the central regions of disk galaxies often with the special case of  $n = 4$  (de Vaucouleurs 1974), though the case of  $n = 1$  has often been used to model the exponential profiles of edge-on disk galaxies (Patterson 1940). Since the utility of Sersic profiles has been evaluated on the classical morphologies of early- and late-type galaxies, systems that significantly deviate from those morphologies will not be adequately fit by this function.

In Paper I, we demonstrated that the Sersic centroid fit, obtained with the galaxy image modeling program GALFIT version 3.0.5 (Peng et al. 2010), is a robust tracer of the peak  $H$ -band brightness, regardless of the residuals at large radii from the centroid. However, in this work

we are also interested in quantifying the global morphologies of the merger systems and the deviations from symmetry that may have arisen from the mergers. Therefore, we redo the analysis here to also include nearby sources so that we can accurately measure the residuals at all radii. First, we run **Source Extractor** (Bertin & Arnouts 1996) on the  $H$ -band images to generate a base list of all the significantly detected ( $> 3\sigma$ ) sources. From this list, we fit Sersic components to all of the detected sources within a  $50 \times 50$  kpc field-of-view (FOV) centered on the SDSS J2000 right ascension and declination of the galaxy, plus a fixed, uniform sky background estimated from a source-free region. The choice of a  $50 \times 50$  kpc FOV allows all nearby contaminating sources to be included in the  $H$ -band fitting box and modeled for all six galaxies. We eliminate some Sersic components from the final fit if they do not centroid on the correct **Source Extractor** position. We test fitting PSFs to the systems, finding that it is necessary only for the faint Southeast source in J1126+2944 (see Paper I for details). While J0952+2552 hosts a Type 1 AGN based on its SDSS spectrum, our analysis in Paper I determined that adding a PSF component does not improve the quality of the fit at a statistically significant level. The  $H$ -band images and results of the GALFIT modeling are shown in Figure 4. As a form of quantifying the level of morphological disturbances in each system we also measured the rotational asymmetry,  $A_{\text{rot}}$ , of each galaxy following the procedure defined in Conselice et al. (2009).

The two Sersic components nearest the SDSS coordinates of the galaxy (in the  $H$ -band reference frame) are considered to be the nuclear components of the merger, with the brightest (based on the  $H$ -band Sersic component magnitudes) referred to as the primary (component 1) and the other as the secondary (component 2). In Table 2 we list the half-light radii ( $r_{e,1}$  and  $r_{e,2}$ ) and Sersic indices ( $n_1$  and  $n_2$ ) for the primary and secondary components, along with  $A_{\text{rot}}$ . In Section 5 we use these parameters to test if the stellar morphologies are correlated with SF properties.

#### 4.2. Color Gradients

From Section 3.1 we see that all six merger systems have small flux contributions in the  $I$ -band (peak wavelength of 8353 Å and  $FWHM = 2555$  Å) and  $B$ -band

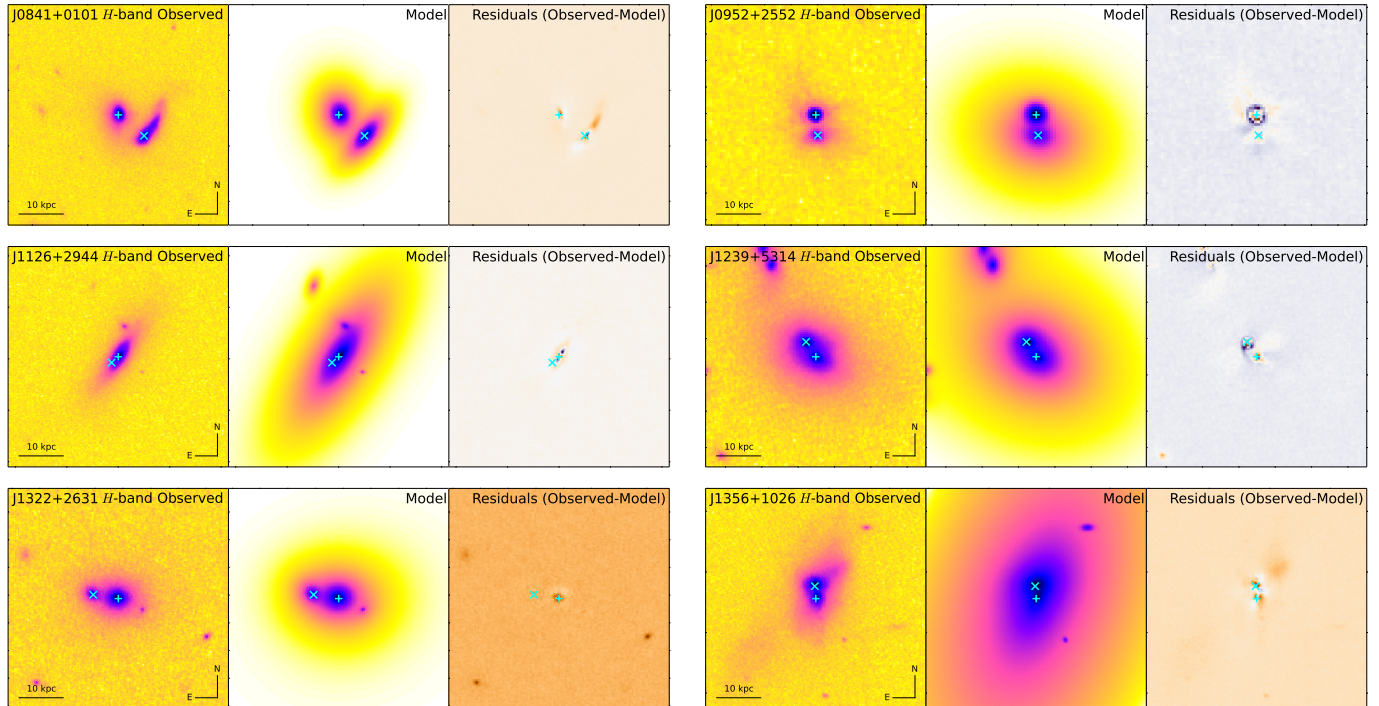


**Figure 4.** From left to right:  $H$ -band image, best GALFIT model of the  $H$ -band image, and the residuals obtained by subtracting the model from the  $H$ -band image. All image panels are displayed over a  $50 \times 50$  kpc FOV (GALFIT fitting box). The cyan ‘+’ and ‘x’ represent the locations of the primary and secondary components of each merger, respectively. The component parameters from these models are analyzed in Section 5.

(peak wavelength of  $4320 \text{ \AA}$  and  $FWHM = 695 \text{ \AA}$ ) from scattered light (0.01–4.49%), and emission lines (<0.14%) and no measurable contribution from AGN-heated dust. As with the  $H$ -band, five of the systems (J0841+0101, J1126+2944, J1239+5314, J1322+2631, and J1356+1026) have small flux contributions in the  $I$ - and  $B$ -bands from AGN light (<0.99%). Also as with the  $H$ -band, while the remaining merger system (J0952+2552) is a Type 1 AGN with a stronger AGN contribution (31.15–63.83%), the AGN flux spatial distribution is described by the  $I$ - and  $B$ -band PSFs and so contributes negligibly to the global  $I$ - and  $B$ -band morphologies. Therefore, the  $I$ - and  $B$ -band galaxy images are dominated by light from stellar continuum emission. This flux corresponds to stellar populations with spectral curves peaking at red optical wavelengths ( $I$ -band) and blue optical/NUV wavelengths ( $B$ -band). These signatures represent relatively old and young stellar populations for the  $I$ - and  $B$ -bands, respectively (Kaviraj et al. 2007) Thus, the difference between the  $I$ - and  $B$ -band galaxy images ( $B-I$ ) can reveal spatial distributions of star-forming regions.

The  $I$ - and  $B$ -band images are the optimal combination for color maps as they have the same pixel scales and the best spatial resolution (seeing FWHMs of  $0''.074$  and  $0''.070$  for the  $I$ - and  $B$ -bands, respectively). To construct  $B-I$  maps, we first register both the  $I$ - and  $B$ -band images (input images) to the same coordinate system as the  $H$ -band image (reference image). We use the astrometric procedure from Barrows et al. (2016), optimized for a small FOV, to register the two images. To combine the images, we follow a procedure similar to the one used in Shangguan et al. (2016) that consists of convolving each image with a Gaussian kernel so that the two images are

at a common resolution of  $FWHM = 0''.080$  and replacing any negative pixel values with interpolated values based on the Gaussian kernel. We then divide pixel values in the  $I$ -band image by those in  $B$ -band image, and compute  $B-I$  using the photometric zeropoints. Figure 5 shows the images of the six mergers in the  $I$ - and  $B$ -band images, along with the  $B-I$  color images.

Finally, we use the `ellipse` task in IRAF to measure the counts and semi-major axes of isophotes from the  $B-I$  color images in linear steps of one pixel from the location of the primary stellar core out to  $3 \times r_e$ , where  $r_e = r_{e,1} + r_{e,2}$  (but no larger than the GALFIT fitting box). We plot  $B-I$  against isophotal semi-major axis in the far right panel of Figure 5. The upper and lower  $5\sigma$  uncertainty bounds are calculated from the isophotal intensity uncertainties generated by `ellipse`. The average  $B-I$  value within  $r_e$ ,  $(B-I)_{\text{avg}}$ , and radial slope of  $B-I$  outside of  $r_e$  calculated from a linear regression of the data,  $\delta(B-I)$ , are listed in Table 2. In Section 5 we use these parameters to determine how the distributions of SF compare with the overall populations of early-type, late-type and peculiar or merging galaxies.

## 5. RESULTS

In this section we describe the main results from the analyses presented in Sections 3 and 4. Our aim is to reveal connections between SF and the merger processes. Specifically, we describe how the SF is spatially distributed within the merging systems (Section 5.1), describe how properties of the stellar populations correlate with global properties of the galaxies (Section 5.2), and describe how the six merger systems compare to their control samples (Section 5.3).

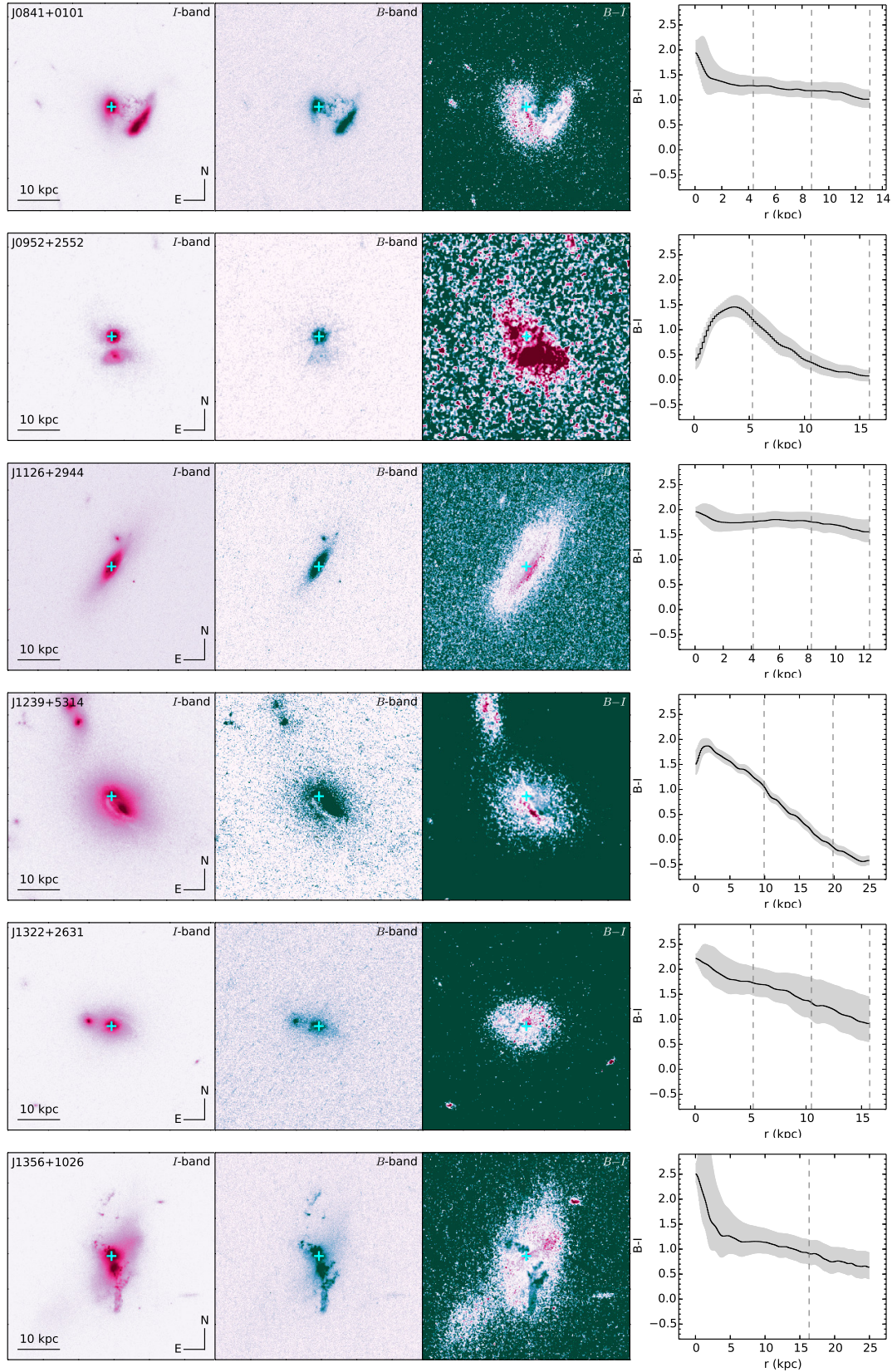


**Figure 5.** From left to right, the three image panels show the following:  $I$ -band image,  $B$ -band image and the  $B-I$  color image with their color scales combined. All image panels are displayed over a  $50 \times 50$  kpc FOV. The cyan cross represents the location of the primary components of each merger. The far right panel shows the  $B-I$  color as a function of physical distance from the primary Sersic component out to  $3r_e$ , with the upper and lower  $5\sigma$  uncertainty bounds indicated by the gray, shaded regions. Starting from 0 kpc, the vertical, black dashed lines represent the 1, 2, and  $3r_e$  radii (for radii of  $< 25$  kpc). Note that, while the radial profiles at small radii have varying slopes due to the presence of AGN continuum emission in some cases, the slopes are negative at large radial distance in all systems. The average  $B-I$  colors and radial slopes are analyzed in Section 5.

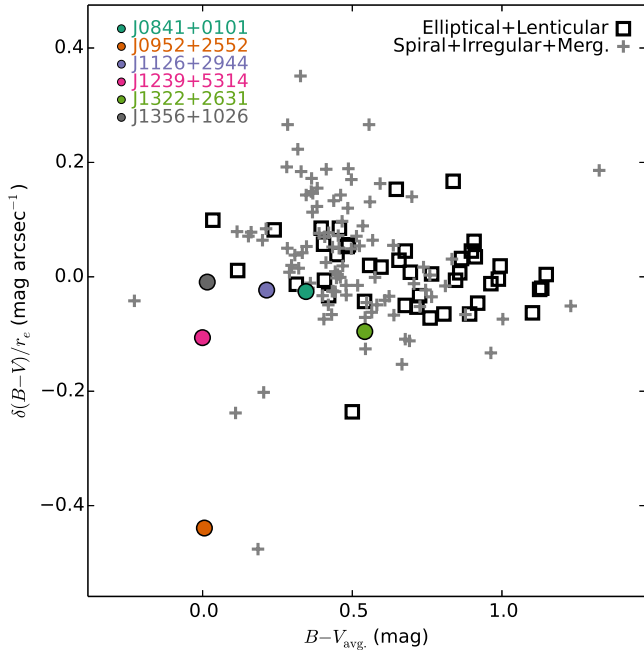


**Figure 6.** Radial  $B-V$  color gradient (outside of  $r_e$ ) as a function of average  $B-V$  (within  $r_e$ ). The six systems from this work are shown as filled circles. Also shown are the elliptical and lenticular systems (black, open squares) and spiral, irregular and merging systems (gray crosses) from Taylor et al. (2005).

### 5.1. Star Formation Is on a Global Scale

While early-type galaxies display relatively shallow radial changes in color (Hunt et al. 1997; Bartholomew et al. 2001; Tamura & Ohta 2003; Cantiello et al. 2005), peculiar (interacting or merging) galaxies are known to produce a wide range of color gradients likely caused by spatial differences in SF and the presence of dust (Taylor et al. 2005). The radial color gradients outside of  $r_e$  for the six mergers,  $\delta(B-I)$ , are shown in Table 2.

Based on their uncertainties, the values of  $\delta(B-I)$  for all six systems are consistent with being negative at  $> 3\sigma$  significance and hence the galaxies become bluer with increasing radial distance from the nucleus. The analysis in Section 4.2 shows that the  $B-I$  colors in these systems are likely dominated by stellar light, and therefore the negative gradients are produced by younger stellar populations and enhanced SF at large radii compared to the nuclear regions. With the exception of J0952+2552 (the system with the largest  $I$ - and  $B$ -band AGN contributions) this result is true even when including the inner  $r_e$  radii and is qualitatively similar to the galaxy colors presented for the late-stage merger sample of Shangguan et al. (2016).

To place our six merger systems within the context of typical galaxy color gradients, in Figure 6 we compare them with the  $B-V$  colors of the sample from Taylor et al. (2005) that consists of 142 nearby galaxies with ground-based UV and optical imaging. To do so, we calculate the  $B-V$  colors (listed in Table 2) using synthetic  $V$ -band magnitudes derived from the SED models. From Figure 6 we see that the mean  $\delta(B-V)$  value of our six merger systems is offset toward negative color gradients from that of the Elliptical+Lenticular sample (by  $1.87\sigma$ ) as expected based on both their merger nature and the av-

erage Sersic indices that suggest late- and intermediate type morphologies. While the Spiral+Irregular+Merger sample has a similar mean  $\delta(B-V)$  value as the Elliptical+Lenticular sample, it has a much larger scatter and hence our merger systems are more consistent with it. However, they still fall on the negative end of the distribution (offset by  $1.28\sigma$ ), showing that our merger systems have relatively negative color gradients compared to typical Spiral+Irregular+Merger galaxies. Therefore, the merger-induced SF is preferentially occurring at large radii in our six systems.

We also acknowledge the possibility that light from star formation at bluer wavelengths is affected by the presence of dust that is not accounted for in our SED models. As a result, the color gradients may be affected by the presence of dust at small radii that obscures some of the nuclear SF. Indeed, circumstantial evidence for this effect includes dust lanes seen in some of the merger systems (Figure 5). In this case, the true effect of merger-induced nuclear SF is higher than that inferred from Figure 6. However, Figure 2 shows that the SFRs and stellar masses from our SED modeling are not systematically under-estimated relative to the dust-corrected values from the SDSS spectra. Additionally, the optical selection of AGN and SF is known to preferentially target galaxies with relatively small amounts of nuclear gas and dust compared to selections at X-ray or IR wavelengths (Ellison et al. 2016) so that these systems are unlikely to be impacted by significant nuclear obscuration. Finally, Figure 6 shows that the mean value of  $(B-V)_{\text{avg.}}$  for our merger systems falls on the blue end of the distribution for the Spiral+Irregular+Merger sample (offset by  $1.32\sigma$ ). Even after removing the two Type 1 AGN (the two systems with the bluest nuclear colors), the mean  $(B-V)_{\text{avg.}}$  value of our merger sample (0.28) is bluer than the Spiral+Irregular+Merger sample (0.48) and thus does not show an excess of red color at small radii steepening the color gradients. Therefore, we ultimately consider the effect of dust reddening to have a negligible impact on our measured negative color gradients and SFRs.

### 5.2. Connection between SF and Morphology

If galaxy interactions and mergers contribute to SF and hence affect the average stellar population ages (i.e. through tidally induced torques on gas), then enhancements in global sSFR may be correlated with morphological properties of the merger. To test this prediction, we compute the differences between sSFR in the merger-selected systems of this work and those of the matched control sample:  $\text{sSFR}_{\text{SED, norm}} = \log[\text{sSFR}_{\text{SED}}] - \log[\text{sSFR}_{\text{ctrl}}]$ . We have chosen to investigate the morphological parameters of mass ratio ( $M_1/M_2$ , from Paper I) and residual asymmetry ( $A_{\text{rot}}$ , from Section 4.1).

To test for correlations between  $\text{sSFR}_{\text{SED}}$  and each of the above parameters  $M_1/M_2$  and  $A_{\text{rot}}$ , we determined the best-fit linear functions for each set of values. Confidence intervals on the slope and intercept are measured by sampling random errors for each data point from a simulated Gaussian distribution with sigma equal to the true error. We iteratively increase the number of simulations until the lower and upper errors, determined from the 34% lower and upper quantiles, respectively, changed by  $< 10\%$ . While we find that the linear slope between

**Table 2**  
Host galaxy properties derived from NIR and optical image modeling.

SDSS Name	$r_{e,1}$	$r_{e,2}$	$n_1$	$n_2$	$A_{\text{rot}}$	$(B-I)_{\text{avg.}}$	$\delta(B-I)$	$(B-V)_{\text{avg.}}$	$\delta(B-V)$
–	(kpc)	(kpc)	–	–	–	(mag)	(mag $r_e^{-1}$ )	(mag)	(mag $r_e^{-1}$ )
(1)	(2)	(3)	(4)	(5)	(6)	(7)	(8)	(9)	(10)
J0841+0101	$1.94 \pm 0.01$	$2.41 \pm 0.01$	$2.29 \pm 0.01$	$1.48 \pm 0.01$	0.98	$1.44^{0.01}_{0.02}$	$-0.026^{0.006}_{0.005}$	$0.35^{0.01}_{0.01}$	$-0.026^{0.005}_{0.005}$
J0952+2552	$0.88 \pm 0.00$	$4.42 \pm 0.12$	$1.18 \pm 0.01$	$2.16 \pm 0.05$	0.52	$1.14^{0.02}_{0.02}$	$-0.439^{0.027}_{0.032}$	$0.01^{0.02}_{0.02}$	$-0.439^{0.029}_{0.031}$
J1126+2944	$3.79 \pm 0.02$	$0.35 \pm 0.04$	$2.40 \pm 0.01$	–	0.27	$1.79^{0.01}_{0.02}$	$-0.023^{0.006}_{0.006}$	$0.21^{0.01}_{0.01}$	$-0.023^{0.005}_{0.005}$
J1239+5314	$3.10 \pm 0.04$	$6.82 \pm 0.08$	$3.46 \pm 0.02$	$2.56 \pm 0.02$	0.74	$1.53^{0.01}_{0.01}$	$-0.106^{0.002}_{0.002}$	$-0.00^{0.01}_{0.01}$	$-0.106^{0.002}_{0.002}$
J1322+2631	$3.25 \pm 0.03$	$1.99 \pm 0.03$	$2.10 \pm 0.01$	$1.79 \pm 0.02$	0.35	$1.93^{0.03}_{0.03}$	$-0.096^{0.011}_{0.011}$	$0.54^{0.04}_{0.03}$	$-0.096^{0.015}_{0.011}$
J1356+1026	$1.99 \pm 0.02$	$14.34 \pm 0.37$	$2.01 \pm 0.01$	$3.86 \pm 0.04$	0.76	$1.28^{0.02}_{0.03}$	$-0.009^{0.003}_{0.002}$	$0.02^{0.02}_{0.03}$	$-0.009^{0.003}_{0.002}$

**Note.** — Column 1: abbreviated SDSS galaxy name; Columns 2-3: effective radii of the primary ( $r_{e,1}$ ) and secondary ( $r_{e,2}$ ) Sersic components; Column 4-5: indices of the primary ( $n_1$ ) and secondary ( $n_2$ ) Sersic components; Column 6: rotational asymmetry index; Column 7: average of  $B-I$  within  $1 \times r_e$  of the primary Sersic component; Column 8: gradient of  $B-I$  within  $1-3 \times r_e$  of the primary Sersic component; Column 9: average of  $B-V$  within  $1 \times r_e$  of the primary Sersic component; Column 10: gradient of  $B-V$  within  $1-3 \times r_e$  of the primary Sersic component.  $r_{e,2}$  (Column 3) and  $n_2$  (Column 5) are not measured for J1126+2944 (Section 4.1).

$\text{sSFR}_{\text{SED,norm}}$  and  $M_1/M_2$  is consistent with a negative correlation, the significance level is  $< 2\sigma$ . On the other hand, the linear slope between  $\text{sSFR}_{\text{SED,norm}}$  and  $A_{\text{rot}}$  is stronger and consistent with a positive correlation at a significance level of  $3.7\sigma$  (top panel of Figure 7).

Since the contamination from scattered light, and hence over-estimates of  $\text{sSFR}_{\text{SED}}$ , are larger among the six merger systems than the control samples (Section 3.3), the values of  $\text{sSFR}_{\text{SED,norm}}$  are likely also over-estimated. To consider this effect, we have corrected each value of  $\text{sSFR}_{\text{SED,norm}}$  by the differences in  $L_{[\text{OIII}]}$  luminosity (assuming that the  $\text{sSFR}_{\text{SED}}$  over-estimates scale directly with the scattered light contribution and hence the AGN luminosity). This correction results in qualitatively similar correlations where the linear slope of  $\text{sSFR}_{\text{SED,norm}}$  with  $M_1/M_2$  is consistent with a negative correlation at a significance level of  $< 2\sigma$ . As with the uncorrected values, the linear slope between  $\text{sSFR}_{\text{SED,norm}}$  and  $A_{\text{rot}}$  is the strongest, consistent with a positive correlation at a significance level of  $3.0\sigma$ . This is shown in the bottom panel of Figure 7. While the only conclusive correlation among either the uncorrected or corrected  $\text{sSFR}_{\text{SED,norm}}$  values is found with  $A_{\text{rot}}$ , both morphological parameters ( $M_1/M_2$  and  $A_{\text{rot}}$ ) evolve with  $\text{sSFR}_{\text{SED,norm}}$  such that more violent mergers correspond to enhanced SF.

### 5.3. Comparison with the Control Samples

From Figure 7 the average value of  $\text{sSFR}_{\text{SED,norm}}$  is  $-0.20 \pm 0.24$  with an offset below zero significant at  $0.8\sigma$ . For comparison, using the corrected values of  $\text{sSFR}_{\text{SED,norm}}$  results in an average of  $-0.57 \pm 0.16$  with an offset below zero significant at  $3.5\sigma$ . These results show that, on average, these merger systems are experiencing comparable (uncorrected values) or lower (corrected values) levels of SF compared to galaxies with similar masses, redshifts, and AGN luminosities that were not selected to be in merger systems.

To understand these effects on SF within the context of the overall galaxy merger process, we compare the normalized values of  $\text{SFR}_{\text{SED}}$  ( $\text{SFR}_{\text{SED,norm}} = \log[\text{SFR}_{\text{SED}}] - \log[\text{SFR}_{\text{ctrl}}]$ ) to those of earlier-stage merger systems. This is shown in Figure 8 where we compare  $\text{SFR}_{\text{SED,norm}}$  for our sample to that of the smallest sep-

aration bin in Figure 3 of Scudder et al. (2012), where values of SFR are based on the SDSS fiber spectroscopy of galaxies with optical emission lines dominated by SF. This bin contains galaxies at a larger average separation of  $\sim 10$  kpc compared to our sample (4.7 kpc). We see that the mean values of our sample are offset below that of Scudder et al. (2012) at significance levels of  $1.7\sigma$  (uncorrected values) and  $5.1\sigma$  (corrected values). Since the average separation of our sample is smaller than that of Scudder et al. (2012), this result suggests that selection for these systems to be in late-stage galaxy mergers is responsible for marginally (uncorrected values) or significantly (corrected values) smaller SFR enhancements relative to slightly earlier-stage mergers. While our sample was selected based upon AGN that dominate the optical emission line spectrum (as opposed to SF dominated optical emission lines in the star-forming sample), the smaller SFR enhancements are unlikely to be due to this selection effect since we have normalized by control samples of AGN selected in the same way.

We note that low-gas fractions among the merger systems would also result in suppressed SF. Indeed, our sample consists of optically selected SDSS AGN that likely have low gas supplies, and hence suppressed SFR, compared to star-forming galaxies (Ellison et al. 2016). However, this selection effect does not impact our analysis since we have normalized the SFRs by control samples of AGN that are also selected optically. Additionally, while Shangguan et al. (2016) suggest that selection of X-ray AGN in galaxy mergers may preferentially find gas-poor systems, this effect is not relevant to our sample since the original AGN identifications were based on optical emission lines. Finally, since the control samples were matched on redshift and mass, both of which strongly affect galaxy gas fractions (Davé et al. 2011), our results are likely unaffected by evolution of the gas fraction.

For the possibility discussed in Section 5.1 where dust is obscuring significant nuclear SF, the true SFR enhancements will be higher than shown in Figure 8 (assuming the control samples are not affected by the same level of nuclear dust obscuration. In this scenario, the SFR enhancements of our late-stage mergers will be more consistent with the larger separation pairs from Scudder et al. (2012). However, as described in Section 5.1, the

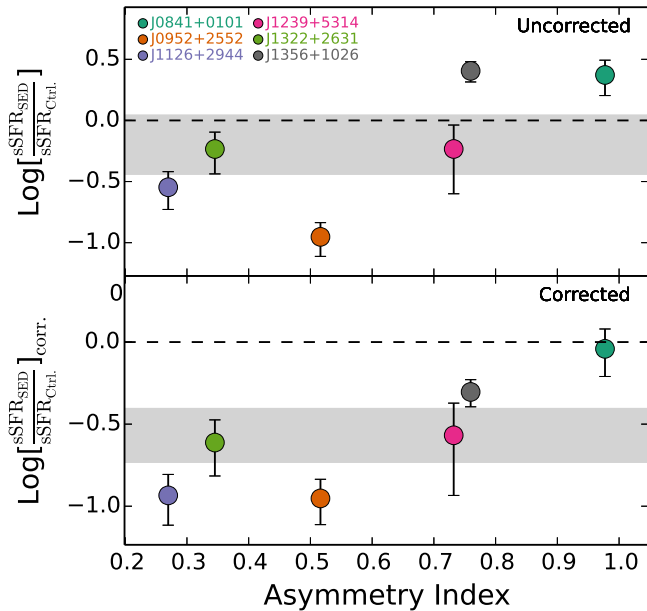


**Figure 7.**  $sSFR_{SED,norm}$  plotted against  $A_{rot}$  for the original values (top) and the values corrected for AGN scattering (bottom). The vertical error bars denote the  $1\sigma$  confidence intervals based on the standard deviation of the control sample. The dashed line represents  $sSFR_{SED} = sSFR_{ctrl}$  while the gray shaded region represents the upper and lower  $1\sigma$  bounds. The uncorrected and corrected values of  $sSFR_{SED,norm}$  increase with  $A_{rot}$  at significance levels of  $3.7\sigma$  and  $3.0\sigma$ , respectively.

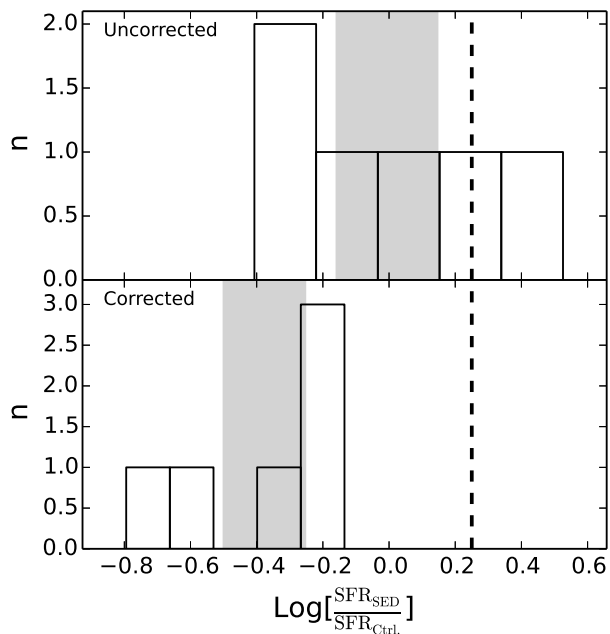


**Figure 8.** Distributions of  $sSFR_{SED,norm}$  for the uncorrected (top) and corrected (bottom) values. The gray-shaded region represents the standard deviation upper and lower bounds. The value from the smallest separation in Figure 3 of Scudder et al. (2012) is shown by the vertical black, dashed line (0.25). Note that the mean value of  $sSFR_{SED,norm}$  is offset below that value from Scudder et al. (2012) by  $1.7\sigma$  (uncorrected) and  $5.1\sigma$  (corrected).

possibility of significant nuclear dust and hidden SF is unlikely. Furthermore, we see the same effect when using the subset of four systems with SFRs from SDSS optical

spectra. Since this is the same measurement procedure for SFRs as in Scudder et al. (2012), both samples will be affected by comparable levels of dust (Ellison et al. 2016).

## 6. DISCUSSION

In this section we synthesize the results from Section 5 to understand how the stellar populations in these systems are affected by the mergers and if their evolution is correlated with that of the SMBHs. Specifically, in Section 6.1 we discuss evidence for merger-induced SF, in Section 6.2 we discuss how the SF may be declining, and in Section 6.3 we discuss how the merger-induced SF and AGN are correlated but may also be offset in time.

### 6.1. Evidence of Merger-induced SF

The  $H$ -band imaging analysis in Section 4.1 provides evidence suggesting the presence of merger-induced morphological disturbances. First, 4/6 systems are classified as major mergers, and 5/6 with mass ratios  $< 7 : 1$  (Comerford et al. 2015). Major galaxy mergers are theoretically predicted and observationally shown to result in significant morphological disturbances. Second, the Sérsic indices for our six systems (Table 2) span the range  $n \sim 1 - 4$ , and two-thirds of them have Sérsic indices in the range  $n \sim 1 - 2.5$ , similar to the late-stage mergers from Shangguan et al. (2016) and typical of late- and intermediate type galaxies. Intermediate-type morphologies are representative of transitional phases often seen in mergers (Fan et al. 2016). There is also only one case of disk structure (J1126+2944), and it is a very minor merger. Hence any disk structure that existed before the mergers was likely destroyed, suggesting that the morphologies are affected by the on-going mergers. These morphological disturbances may be connected to the evidence of on-going global SF presented in Section 5.1. This connection is quantified in Section 5.2 where the significant positive correlation between enhanced sSFR and residual asymmetry suggests that the SF is dependent on the level of tidal disturbances.

While we also see marginal evidence for enhanced sSFRs in more major mergers, the correlation is statistically weak ( $< 2\sigma$ ) and hence we do not claim that it is real. The absence of such a correlation would be consistent with previous observations that have found minor mergers to play a role comparable to or greater than that of major mergers in triggering SF (Woods & Geller 2007; Shabala et al. 2012; Kaviraj 2014; Willett et al. 2015). Instead, the morphological asymmetries may be more direct tracers of the gravitational tidal forces on the host galaxy potential, a parameter that has been shown to affect SF in mergers (Woods & Geller 2007). Hence, they are imprinted with the past dynamics of the merger and lead to the strong correlation with sSFR enhancement seen in Figure 7. This connection between mergers and SF is consistent with results for earlier stage pairs (Ellison et al. 2008; Scudder et al. 2012; Patton et al. 2013), and our sample shows that this connection persists at separations of  $\sim 2$  kpc.

### 6.2. Merger-induced Global SF May Be Declining

In Section 5.3 we showed that the average sSFRs of our AGN sample are comparable to or lower than those

of the control sample (Figure 7) and that the average SFR enhancements are lower than those of earlier-stage mergers of star-forming galaxies by  $1 - 5\sigma$  (Figure 8). Furthermore, we showed that the relative lack of SFR enhancements are not due to dust obscuration hiding nuclear SF (Section 5.1) or due to a selection bias of AGN dominated optical emission lines (Section 5.3).

Therefore, compared to the star-forming samples, the SF in our sample may correspond to starbursts induced by the galaxy interaction at a relatively earlier stage and that occurred on larger physical scales (Patton et al. 2013). Indeed, our analysis in Section 5.1 shows that the merger-induced SF is preferentially occurring at large radii. On the other hand, the SFRs used in the star-forming samples are known to be centrally concentrated (Patton et al. 2011). Therefore, we are likely viewing these late-stage mergers as the global SFRs are declining relative to the earlier-stage systems. This scenario is predicted by numerical simulations of mergers that find a peak in global SFR occurs a few Myrs after the first pericentric passage when the nuclear separation ranges from 10 – 100 kpc (Cox et al. 2008; Kim et al. 2009; Teyssier et al. 2010; Scudder et al. 2012; Stickley & Canalizo 2014; Renaud et al. 2014). As the merger progresses to nuclear separations below 10 kpc (corresponding to the separations in our sample), the global SF has mostly completed (Patton et al. 2011) and is predicted to be relatively unaffected compared to the nuclear SFR (Hopkins et al. 2008; Capelo et al. 2015).

The nuclear SFR may continue to rise toward later merger stages (potentially peaking post-coalescence) when the AGN also becomes more active, leading to correlated activity (Li et al. 2008). Indeed, a subsequent rise in nuclear SF that corresponds temporally to the AGN peak luminosity is numerically predicted (Hopkins 2012), and simulations show that this nuclear SF can account for a significant fraction of the overall galaxy SFR (Capelo et al. 2015; Volonteri et al. 2015). Therefore, the nuclear SFR enhancements in our sample may continue rising toward later merger stages and eventually peak after nuclear coalescence.

We note that the offset in Figure 8 of  $1.7\sigma$  does not robustly eliminate the possibility that the normalized SFRs for our sample are in fact similar to those of the larger separation pairs. However, we can still confidently rule out the possibility that the normalized SFRs in our sub  $-10$  kpc separation sample are elevated relative to larger separation pairs. Thus when viewed together, the studies are consistent with a scenario in which the enhancements in global SFR subside below  $\sim 10$  kpc.

### 6.3. Connection between SF and AGN in Late-stage Galaxy Mergers

In this section we investigate the connection between SF and AGN triggering in our six late-stage merger systems. Specifically, we examine the connection between merger-induced SF (Section 6.3.1) but also discuss possible evidence for a delay between the two (Section 6.3.2).

#### 6.3.1. Both SF and AGN Are Merger-triggered

The discussion in Section 6.1 shows that enhancements in sSFR are strongest in more disturbed systems, a result strongly predicted by observational results from merger

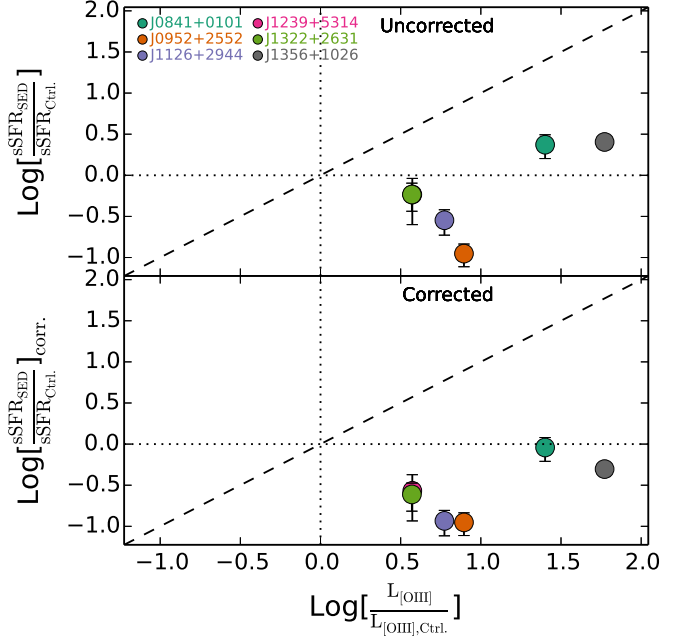


**Figure 9.**  $sSFR_{SED,norm}$  plotted against  $L_{[OIII],norm}$  for the uncorrected (top) and corrected (bottom) values. The dashed line represents the one-to-one relation. The horizontal and vertical dotted lines represent  $sSFR_{SED}=sSFR_{ctrl}$  and  $L_{[OIII]}=L_{[OIII],ctrl}$ , respectively. The uncorrected and corrected values of  $sSFR_{SED,norm}$  increase with  $L_{[OIII],norm}$  at significance levels of  $3.7\sigma$  and  $2.2\sigma$ , respectively.

samples at earlier stages (Ellison et al. 2008; Patton et al. 2011; Scudder et al. 2012). Furthermore, some observational evidence suggests that these same violent mergers are more likely to trigger AGN as well (Treister et al. 2012; Glikman et al. 2015). From these two observations follows the prediction that merger-induced SF and AGN scale with each other. However, as mentioned in Section 1, finding observational evidence of this correlation has proven difficult. Numerical simulations from Volonteri et al. (2015) predict that the link between global SFR and SMBH accretion rate only emerges among their late-stage merger sample. Indeed, our sample contains global SFRs that are consistent with the SFRs of the Volonteri et al. (2015) late-stage merger sample ( $1 - 10 M_{\odot} \text{ yr}^{-1}$ ) and hence is suitable for testing this prediction.

To do so, we have created control samples for each of the AGN in a manner identical to that of Section 3.3 except that we have excluded the  $L_{[OIII]}$  matching criteria so that we can compare the AGN bolometric luminosities (assumed to be proportional to  $L_{[OIII]}$ ). We then compute the normalized values of  $L_{[OIII]}$  ( $L_{[OIII],norm}=\log[L_{[OIII]}]-\log[L_{[OIII],ctrl}]$ ) and plot  $L_{[OIII],norm}$  against  $sSFR_{SED,norm}$  in Figure 9. We see that all values of normalized  $L_{[OIII]}$  are significantly above unity, a result that is likely due to the selection of bright AGN for *Chandra* detections (see Section 2). We test for a correlation between normalized  $L_{[OIII]}$  and normalized sSFR using the same procedure as in Section 5.2, finding positive correlations at significance levels of  $3.7\sigma$  and  $2.2\sigma$  for the uncorrected and corrected samples, respectively (we note that the correlation is driven primarily by the two galaxies with the brightest

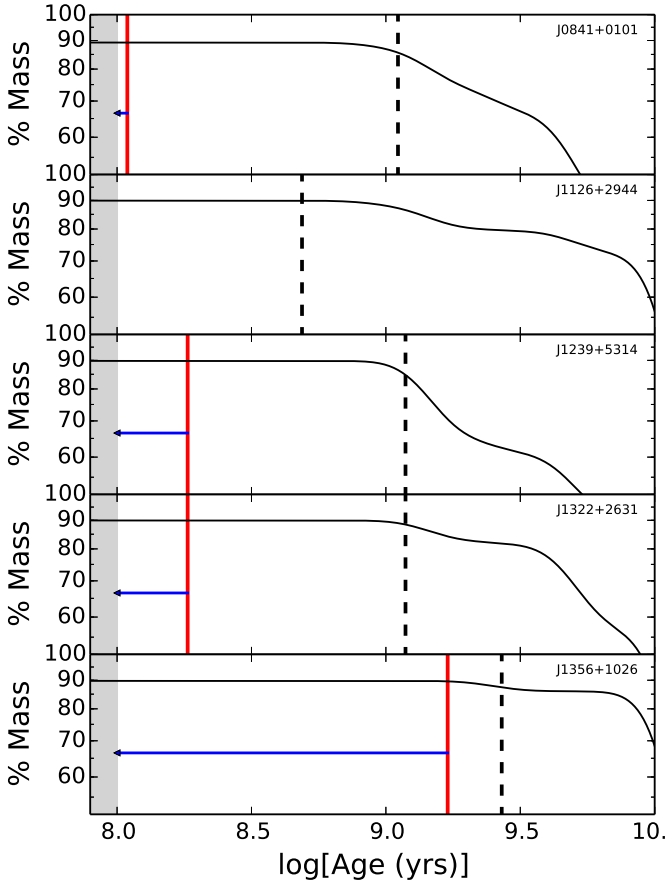


**Figure 10.** Delays between the peak of merger triggered SF and the onset of merger triggered AGN for the five galaxies with reliable STARLIGHT models. The solid black curve represents the fraction of mass assembled from star formation as a function of lookback time based on the ages of stellar bases in the best-fit STARLIGHT models. The vertical dashed, black line represents the estimated onset of the merger, the vertical solid, red line represents the estimate peak of global SF, and the gray shaded region represents the estimated AGN duty cycle. The horizontal blue arrow represents the temporal delay between the estimated peak of global SF and the onset of the AGN duty cycle in cases where a delay is detected. All times and ages are in the galaxy’s reference frame.

AGN). Therefore, we see evidence that enhancements in sSFR correspond to enhancements in AGN luminosity.

### 6.3.2. Time Delay between Merger-induced SF and AGN

While Figure 9 shows that the normalized values of  $L_{[\text{OIII}]}$  are all significantly above unity, the average value for the normalized sSFRs is less than unity (discussed in Section 5.3). This significant difference in the relative enhancements is consistent with the implication from Section 6.2 that the merger-induced enhancement in sSFR happened at an earlier phase in the merger than for the AGN. Moreover, this result is qualitatively consistent with the detection of delays between SF and AGN in observational work (Schawinski et al. 2009; Wild et al. 2010; Kaviraj et al. 2015b; Shabala et al. 2017) and theoretical work (Hopkins 2012; Capelo et al. 2015).

To directly compare our inferred delays with these works, we create a timeline of stellar mass assembly using the best-fitting combination of STARLIGHT stellar templates following the procedure described in Cid

Fernandes et al. (2007). For each of the stellar population bases used by our STARLIGHT modeling the implicit assumption exists that all of the mass was created in a instantaneous burst of SF (Fernandes et al. 2005). Therefore, for a given look-back time, the total stellar mass formed through SF is the cumulative sum of the masses for all stellar populations with ages equal to or less than that time. Examining this cumulative sum as a function of stellar population age shows the timescale (in the galaxy’s reference frame) over which stellar mass is assembled due to SF. These timelines are shown in Figure 10 for each of the five galaxies with reliable STARLIGHT models, where we have normalized the cumulative mass by the total mass from all stellar bases so that it represents the mass fraction.

To place the peak in global SF on the timeline we assume that it occurs  $10^9$  yrs after the merger begins (this value corresponds to an upper estimate based on the range of values from simulations (300 – 700 Myrs) and is typically a few hundred Myrs after the first pericentric passage (Scudder et al. 2012; Stickley & Canalizo 2014; Capelo et al. 2015). The merger onset corresponds to the time when the fraction of remaining mass to be assembled equals the fraction of mass assembled by merger-induced SF ( $f_{\text{M,merg.}}$ ). We estimate a conservatively low value of  $f_{\text{M,merg.}}$  from the ‘burst efficiency’ function (Cox et al. 2008), the merger mass ratios, and a low estimate of 10% for the galaxy gas mass fractions (Jaskot et al. 2015). The lookback times of the merger onset are shown in Figure 10, and they represent conservatively low estimates.

Since the AGN are observed to currently be active, the maximum lookback time for their merger-induced onset is  $10^8$  yrs based on typical estimates of AGN duty cycles (Parma et al. 2007; Shulevski et al. 2015). Figure 10 shows that four of the five systems with reliable STARLIGHT models (J0841+0101, J1239+5314, J1322+2631, and J1356+1026) have lower limits on the peak global SF lookback times ( $\log[t_{\text{age,SDSS}}(\text{yrs})] = 8.04 - 9.23$ ) that are greater than the AGN duty cycle of  $10^8$  yrs. These times correspond to lower estimates of the delay between the global SF peak and AGN onset of  $\log[t_{\text{age,SDSS}}(\text{yrs})] = 6.96 - 9.20$ , with an average value of  $4.4 \times 10^8$  yrs.

We note that the average value of  $4.4 \times 10^8$  yrs is similar to the delays of 100 – 400 Myrs measured by previous works (Schawinski et al. 2009; Wild et al. 2010; Kaviraj et al. 2015b; Shabala et al. 2017). However, the average delay of our sample represents a lower estimate and hence the true value is likely to be longer. We hypothesize that our measured time delays are longer because they exclude post-merger systems for which subsequent bursts of small-scale SF may occur after nuclear coalescence.

## 7. CONCLUSIONS

We have analyzed the *HST* imaging and archival photometry and spectra for a sample of six late-stage galaxy mergers hosting AGN. In Paper I, we put constraints on the efficiency of the mergers for triggering the AGN. In this paper, our aim is to understand the effects of the mergers on evolution of the host galaxy stellar populations and if it is correlated with SMBH growth. We have used *HST* imaging to quantify the tidal disturbances in the stars and the spatial distribution of star formation.

We have used the photometric and spectral data to measure the star formation rates, stellar masses, and stellar ages of the systems. Our conclusions are as follows:

1. With increasing radial distance from the nuclei the merger systems become increasingly dominated by younger stellar populations. Furthermore, the radial color gradients are on the negative end of the distribution for typical galaxy mergers suggesting that the majority of merger-induced star formation is occurring on a galaxy-wide (global) scale.
2. The specific star formation rates, normalized by matched control samples, are positively correlated with asymmetries in the NIR images. This result suggests that enhancements in the specific star formation rates are strongly coupled to the level of tidal disturbances. Hence, the elevated specific star formation rates are likely to be merger-induced.
3. The normalized star formation rates are on average lower than those from larger separation (earlier merger stage) galaxy pairs by  $> 1\sigma$  and potentially by  $\sim 5\sigma$  when estimates of scattered AGN flux are taken into account. An offset toward smaller star formation rate enhancements compared to larger separation pairs is consistent with galaxy merger simulations predicting a decline in global star formation rates below separations of  $\sim 10$  kpc.
4. Enhancements in specific star formation rates are positively correlated with enhanced AGN luminosity, suggesting that both values are mutually triggered by the merger events. This result is consistent with predictions from late-stage merger simulations and with extrapolations from previous studies of larger separation pairs that imply AGN luminosity and star formation are both enhanced in galaxy mergers.
5. The average enhancement in AGN luminosity is significantly larger than that of the specific star formation rates, suggesting that the level of AGN triggering in these late-stage systems exceeds that of star formation. Furthermore, in four out of five systems we see evidence for an average difference of  $\gtrsim 10^8$  yrs between the peak of global, merger-induced star formation and the onset of SMBH accretion. Both results are consistent with delays between merger-triggered star formation and AGN.

Support for this work was provided by NASA through Chandra Award Number GO2-13130A issued by the Chandra X-ray Observatory Center, which is operated by the Smithsonian Astrophysical Observatory for and on behalf of NASA under contract NAS8-03060. Support for HST program number GO-12754 was provided by NASA through a grant from the Space Telescope Science Institute, which is operated by the Association of Universities for Research in Astronomy, Inc., under NASA contract NAS5-26555. The scientific results reported in this article are based in part on observations made by the Chandra X-ray Observatory, and this research has made use of software provided by the Chandra X-ray Center in the application packages CIAO, ChIPS, and Sherpa.

The results reported here are also based on observations made with the NASA/ESA Hubble Space Telescope, obtained at the Space Telescope Science Institute, which is operated by the Association of Universities for Research in Astronomy, Inc., under NASA contract NAS 5-26555. These observations are associated with program number GO-12754.

## REFERENCES

- Antonucci, R. R. J., & Miller, J. S. 1985, *ApJ*, 297, 621  
 Assef, R. J., et al. 2010, *AJ*, 713, 970  
 Baldwin, J. A., Phillips, M. M., & Terlevich, R. 1981, *PASP*, 93, 5  
 Barnes, J. E., & Hernquist, L. E. 1991, *ApJ*, 370, L65  
 Barrows, R. S., Comerford, J. M., Greene, J. E., & Pooley, D. 2016, *ApJ*, 829, 37  
 —. 2017, *ApJ*, 838, 129  
 Bartholomew, L. J., Rose, J. A., Gaba, A. E., & Caldwell, N. 2001, *AJ*, 122, 2913  
 Bell, E. F., McIntosh, D. H., Katz, N., & Weinberg, M. D. 2003, *ApJS*, 149, 289  
 Bentz, M. C., Peterson, B. M., Pogge, R. W., & Vestergaard, M. 2009, *The Astrophysical Journal Letters*, 694, L166  
 Bertin, E., & Arnouts, S. 1996, *A&AS*, 117, 393  
 Brinchmann, J., Charlot, S., White, S. D. M., Tremonti, C., Kauffmann, G., Heckman, T., & Brinkmann, J. 2004, *MNRAS*, 351, 1151  
 Bruzual, G., & Charlot, S. 2003, *MNRAS*, 344, 1000  
 Canalizo, G., & Stockton, A. 2001, *ApJ*, 555, 719  
 Cantiello, M., Blakeslee, J. P., Raimondo, G., Mei, S., Brocato, E., & Capaccioli, M. 2005, *ApJ*, 634, 239  
 Capelo, P. R., Dotti, M., Volonteri, M., Mayer, L., Bellovary, J. M., & Shen, S. 2016, *ArXiv e-prints*  
 Capelo, P. R., Volonteri, M., Dotti, M., Bellovary, J. M., Mayer, L., & Governato, F. 2015, *MNRAS*, 447, 2123  
 Cardelli, J. A., Clayton, G. C., & Mathis, J. S. 1989, *ApJ*, 345, 245  
 Cid Fernandes, R., Asari, N. V., Sodr e, L., Stasińska, G., Mateus, A., Torres-Papaqui, J. P., & Schoenell, W. 2007, *MNRAS*, 375, L16  
 Cid Fernandes, R., Gu, Q., Melnick, J., Terlevich, E., Terlevich, R., Kunth, D., Rodrigues Lacerda, R., & Jørgensen, B. 2004, *MNRAS*, 355, 273  
 Comerford, J. M., & Greene, J. E. 2014, *ApJ*, 789, 112  
 Comerford, J. M., Pooley, D., Barrows, R. S., Greene, J. E., Zakamska, N. L., Madejski, G. M., & Cooper, M. C. 2015, *ApJ*, 806, 219  
 Conselice, C. J., Yang, C., & Bluck, A. F. L. 2009, *MNRAS*, 394, 1956  
 Cox, T. J., Jonsson, P., Somerville, R. S., Primack, J. R., & Dekel, A. 2008, *MNRAS*, 384, 386  
 Cullen, H., Alexander, P., & Clemens, M. 2006, *MNRAS*, 366, 49  
 Dav e, R., Finlator, K., & Oppenheimer, B. D. 2011, *Monthly Notices of the Royal Astronomical Society*, 416, 1354  
 Davies, R. I., M uller S anchez, F., Genzel, R., Tacconi, L. J., Hicks, E. K. S., Friedrich, S., & Sternberg, A. 2007, *ApJ*, 671, 1388  
 de Vaucouleurs, G. 1974, in *IAU Symposium, Vol. 58, The Formation and Dynamics of Galaxies*, ed. J. R. Shakeshaft, 335  
 Di Matteo, T., Springel, V., & Hernquist, L. 2005, *Nature*, 433, 604  
 Diamond-Stanic, A. M., & Rieke, G. H. 2012, *ApJ*, 746, 168  
 Draine, B. T. 2003, *ApJ*, 598, 1017  
 Duc, P.-A., Brinks, E., Wink, J. E., & Mirabel, I. F. 1997, *A&A*, 326, 537  
 Ellison, S. L., Patton, D. R., Mendel, J. T., & Scudder, J. M. 2011, *MNRAS*, 418, 2043  
 Ellison, S. L., Patton, D. R., Simard, L., & McConnachie, A. W. 2008, *AJ*, 135, 1877  
 Ellison, S. L., Teimoorinia, H., Rosario, D. J., & Mendel, J. T. 2016, *MNRAS*, 458, L34  
 Elmegreen, D. M., Elmegreen, B. G., Kaufman, M., Sheth, K., Struck, C., Thomasson, M., & Brinks, E. 2006, *ApJ*, 642, 158  
 Engel, H., Davies, R. I., Genzel, R., Tacconi, L. J., Sturm, E., & Downes, D. 2011, *ApJ*, 729, 58

- Fernandes, R. C., Mateus, A., Sodr e, L., Stasi nska, G., & Gomes, J. M. 2005, *Monthly Notices of the Royal Astronomical Society*, 358, 363
- Ferrarese, L., & Merritt, D. 2000, *ApJ*, 539, L9
- Gebhardt, K., et al. 2000, *ApJ*, 539, L13
- Georgakakis, A., et al. 2009, *MNRAS*, 397, 623
- Glikman, E., Simmons, B., Maily, M., Schawinski, K., Urry, C. M., & Lacy, M. 2015, *ApJ*, 806, 218
- Gordon, K. D., & Clayton, G. C. 1998, *ApJ*, 500, 816
- Graham, A. W., & Driver, S. P. 2005, *PASA*, 22, 118
- Greene, J. E., Pooley, D., Zakamska, N. L., Comerford, J. M., & Sun, A.-L. 2014, *ApJ*, 788, 54
- G lztekin, K., et al. 2009, *ApJ*, 698, 198
- Guo, R., Hao, C.-N., Xia, X. Y., Mao, S., & Shi, Y. 2016, *ApJ*, 826, 30
- Hancock, M., Smith, B. J., Struck, C., Giroux, M. L., & Hurlock, S. 2009, *AJ*, 137, 4643
- Heckman, T. M., & Best, P. N. 2014, *ARA&A*, 52, 589
- Heckman, T. M., Kauffmann, G., Brinchmann, J., Charlot, S., Tremonti, C., & White, S. D. M. 2004, *ApJ*, 613, 109
- Hernquist, L. 1989, *Nature*, 340, 687
- Hopkins, P. F. 2012, *MNRAS*, 420, L8
- Hopkins, P. F., Hernquist, L., Cox, T. J., Di Matteo, T., Martini, P., Robertson, B., & Springel, V. 2005, *ApJ*, 630, 705
- Hopkins, P. F., Hernquist, L., Cox, T. J., & Kere s, D. 2008, *ApJS*, 175, 356
- Hunt, L. K., Malkan, M. A., Salvati, M., Mandolesi, N., Palazzi, E., & Wade, R. 1997, *ApJS*, 108, 229
- Jaskot, A. E., Oey, M. S., Salzer, J. J., Van Sistine, A., Bell, E. F., & Haynes, M. P. 2015, *ApJ*, 808, 66
- Jogee, S., et al. 2009, *ApJ*, 697, 1971
- Joseph, R. D., & Wright, G. S. 1985, *MNRAS*, 214, 87
- Kauffmann, G., et al. 2003, *MNRAS*, 346, 1055
- Kaviraj, S. 2014, *MNRAS*, 440, 2944
- Kaviraj, S., Rey, S.-C., Rich, R., Yoon, S.-J., & Yi, S. 2007, *Monthly Notices of the Royal Astronomical Society: Letters*, 381, L74
- Kaviraj, S., Shabala, S. S., Deller, A. T., & Middelberg, E. 2015a, *MNRAS*, 454, 1595
- , 2015b, *MNRAS*, 452, 774
- Keel, W. C., Kennicutt, Jr., R. C., Hummel, E., & van der Hulst, J. M. 1985, *AJ*, 90, 708
- Kewley, L. J., Groves, B., Kauffmann, G., & Heckman, T. 2006, *MNRAS*, 372, 961
- Kim, J.-h., Wise, J. H., & Abel, T. 2009, *ApJ*, 694, L123
- Kishimoto, M. 1999, *ApJ*, 518, 676
- Kishimoto, M., Antonucci, R., Cimatti, A., Hurt, T., Dey, A., van Breugel, W., & Spinrad, H. 2001, *ApJ*, 547, 667
- Knapen, J. H., & Cisternas, M. 2015, *ApJ*, 807, L16
- Knapen, J. H., Cisternas, M., & Querejeta, M. 2015, *MNRAS*, 454, 1742
- Kocevski, D. D., et al. 2012, *ApJ*, 744, 148
- Lee, J. C., et al. 2009, *ApJ*, 706, 599
- Li, C., Kauffmann, G., Heckman, T. M., White, S. D. M., & Jing, Y. P. 2008, *MNRAS*, 385, 1915
- Madau, P., & Dickinson, M. 2014, *ARA&A*, 52, 415
- Madau, P., Pozzetti, L., & Dickinson, M. 1998, *ApJ*, 498, 106
- Mannucci, F., Basile, F., Poggianti, B. M., Cimatti, A., Daddi, E., Pozzetti, L., & Vanzani, L. 2001, *MNRAS*, 326, 745
- Marconi, A., & Hunt, L. K. 2003, *ApJ*, 589, L21
- Martin, C., et al. 2003, in *Society of Photo-Optical Instrumentation Engineers (SPIE) Conference Series*, Vol. 4854, *Society of Photo-Optical Instrumentation Engineers (SPIE) Conference Series*, ed. J. C. Blades & O. H. W. Siegmund, 336–350
- Mechtley, M., et al. 2015, *ArXiv e-prints*
- Mezcua, M., Lobanov, A. P., Chavushyan, V. H., & Le on-Tavares, J. 2011, *A&A*, 527, A38
- Mihos, J. C., & Hernquist, L. 1994, *ApJ*, 425, L13
- , 1996, *ApJ*, 464, 641
- Nevin, R., Comerford, J. M., M ller-S nchez, F., Barrows, R. S., & Cooper, M. C. 2017, *ArXiv e-prints*
- Obied, G., Zakamska, N. L., Wylezalek, D., & Liu, G. 2016, *MNRAS*, 456, 2861
- Parma, P., Murgia, M., de Ruiter, H. R., Fanti, R., Mack, K.-H., & Govoni, F. 2007, *A&A*, 470, 875
- Patterson, F. S. 1940, *Harvard College Observatory Bulletin*, 914, 9
- Patton, D. R., Ellison, S. L., Simard, L., McConnachie, A. W., & Mendel, J. T. 2011, *MNRAS*, 412, 591
- Patton, D. R., Torrey, P., Ellison, S. L., Mendel, J. T., & Scudder, J. M. 2013, *MNRAS*, 433, L59
- Peng, C. Y., Ho, L. C., Impey, C. D., & Rix, H.-W. 2010, *AJ*, 139, 2097
- Renaud, F., Bournaud, F., Kraljic, K., & Duc, P.-A. 2014, *MNRAS*, 442, L33
- Reyes, R., et al. 2008, *AJ*, 136, 2373
- Richards, G. T., et al. 2006, *ApJS*, 166, 470
- Rosario, D. J., et al. 2012, *A&A*, 545, A45
- Sanders, D. B., & Mirabel, I. F. 1996, *ARA&A*, 34, 749
- Sanders, D. B., Soifer, B. T., Elias, J. H., Madore, B. F., Matthews, K., Neugebauer, G., & Scoville, N. Z. 1988a, *ApJ*, 325, 74
- Sanders, D. B., Soifer, B. T., Elias, J. H., Neugebauer, G., & Matthews, K. 1988b, *ApJ*, 328, L35
- Satyapal, S., Ellison, S. L., McAlpine, W., Hickox, R. C., Patton, D. R., & Mendel, J. T. 2014, *MNRAS*, 441, 1297
- Schawinski, K., Thomas, D., Sarzi, M., Maraston, C., Kaviraj, S., Joo, S.-J., Yi, S. K., & Silk, J. 2007, *MNRAS*, 382, 1415
- Schawinski, K., Virani, S., Simmons, B., Urry, C. M., Treister, E., Kaviraj, S., & Kushkuley, B. 2009, *ApJ*, 692, L19
- Schneider, D. P., et al. 2010, *AJ*, 139, 2360
- Scudder, J. M., Ellison, S. L., Torrey, P., Patton, D. R., & Mendel, J. T. 2012, *MNRAS*, 426, 549
- Sersic, J. L. 1968, *Atlas de galaxias australes*
- Shabala, S. S., Deller, A., Kaviraj, S., Middelberg, E., Turner, R. J., Ting, Y. S., Allison, J. R., & Davis, T. A. 2017, *MNRAS*, 464, 4706
- Shabala, S. S., et al. 2012, *MNRAS*, 423, 59
- Shangguan, J., Liu, X., Ho, L. C., Shen, Y., Peng, C. Y., Greene, J. E., & Strauss, M. A. 2016, *ApJ*, 823, 50
- Shulevski, A., et al. 2015, *A&A*, 583, A89
- Simmons, B. D., Urry, C. M., Schawinski, K., Cardamone, C., & Glikman, E. 2012, *ApJ*, 761, 75
- Smith, B. J., et al. 2008, *AJ*, 135, 2406
- Somerville, R. S., Primack, J. R., & Faber, S. M. 2001, *MNRAS*, 320, 504
- Springel, V., Di Matteo, T., & Hernquist, L. 2005a, *ApJ*, 620, L79
- , 2005b, *ApJ*, 620, L79
- Stickley, N. R., & Canalizo, G. 2014, *ApJ*, 786, 12
- Tamura, N., & Ohta, K. 2003, *AJ*, 126, 596
- Taylor, V. A., Jansen, R. A., Windhorst, R. A., Odewahn, S. C., & Hibbard, J. E. 2005, *ApJ*, 630, 784
- Teyssier, R., Chapon, D., & Bournaud, F. 2010, *ApJ*, 720, L149
- Treister, E., Schawinski, K., Urry, C. M., & Simmons, B. D. 2012, *ApJ*, 758, L39
- Tsuzuki, Y., Kawara, K., Yoshii, Y., Oyabu, S., Tanab e, T., & Matsuoka, Y. 2006, *ApJ*, 650, 57
- Vanden Berk, D. E., et al. 2001, *AJ*, 122, 549
- V eron-Cetty, M.-P., Joly, M., & V eron, P. 2004, *A&A*, 417, 515
- Villforth, C., et al. 2014, *MNRAS*, 439, 3342
- , 2016, *ArXiv e-prints*
- Volonteri, M., Capelo, P. R., Netzer, H., Bellovary, J., Dotti, M., & Governato, F. 2015, *MNRAS*, 452, L6
- Wild, V., Heckman, T., & Charlot, S. 2010, *MNRAS*, 405, 933
- Wild, V., Kauffmann, G., Heckman, T., Charlot, S., Lemson, G., Brinchmann, J., Reichard, T., & Pasquali, A. 2007, *MNRAS*, 381, 543
- Willett, K. W., et al. 2015, *MNRAS*, 449, 820
- Woods, D. F., & Geller, M. J. 2007, *The Astronomical Journal*, 134, 527
- Wright, E. L., et al. 2010, *AJ*, 140, 1868
- Wylezalek, D., Zakamska, N. L., Liu, G., & Obied, G. 2016, *MNRAS*, 457, 745
- Zakamska, N. L., et al. 2005, *AJ*, 129, 1212
- , 2006, *AJ*, 132, 1496